A non-conducting role of the $Ca_v1.4$ Ca^{2+} channel drives homeostatic plasticity at the cone photoreceptor synapse

J. Wesley Maddox[1,6], Gregory J. Ordemann[1,6], Juan de la Rosa Vázquez [1], Angie Huang,[1] Christof Gault,[1] Serena R. Wisner[2,3], Kate Randall[1], Daiki Futagi[4], Nihal A. Salem[1], R. Dayne Mayfield[1], Boris V. Zemelman[1], Steven H. DeVries[4], Mrinalini Hoon[2,5] and Amy Lee[1*]

[1]Dept of Neuroscience, University of Texas-Austin, Austin, TX 78712, USA

[2]Dept. of Ophthalmology and Visual Sciences, University of Wisconsin- Madison, Madison, WI, 53706, USA

[3]Neuroscience Training Program, University of Wisconsin-Madison, Madison WI 53706 USA

[4]Dept. of Ophthalmology, Northwestern University Feinberg School of Medicine, Chicago, IL, 60611, USA

[5] McPherson Eye Research Institute, Madison WI 53706 USA

[6]These authors contributed equally

[*]Corresponding author, email: amy.lee1@austin.utexas.edu

ABSTRACT

In congenital stationary night blindness type 2 (CSNB2)—a disorder involving the $Ca_v1.4$ (L-type) Ca^{2+} channel—visual impairment is mild considering that $Ca_v1.4$ mediates synaptic release from rod and cone photoreceptors. Here, we addressed this conundrum using a $Ca_v1.4$ knockout (KO) mouse and a knock-in (G369i KI) mouse expressing a non-conducting $Ca_v1.4$. Surprisingly, Ca_v3 (T-type) Ca^{2+} currents were detected in cones of G369i KI mice and $Ca_v1.4$ KO mice but not in cones of wild-type mouse, ground squirrel, and macaque retina. Whereas $Ca_v1.4$ KO mice are blind, G369i KI mice exhibit normal photopic (i.e., cone-mediated) visual behavior. Cone synapses, which fail to form in $Ca_v1.4$ KO mice, are present, albeit enlarged, and with some errors in postsynaptic wiring in G369i KI mice. While $Ca_v1.4$ KO mice lack evidence of cone synaptic responses, electrophysiological recordings in G369i KI mice revealed nominal transmission from cones to horizontal cells and bipolar cells. In CSNB2, we propose that Ca_v3 channels maintain cone synaptic output provided that the nonconducting role of $Ca_v1.4$ in cone synaptogenesis remains intact. Our findings reveal an unexpected form of homeostatic plasticity that relies on a non-canonical role of an ion channel.

KEYWORDS: photoreceptor, Ca^{2+} channel, ribbon synapse, retina, synaptogenesis

INTRODUCTION

At the first synapse in the visual pathway, graded electrical signals produced in rod and cone photoreceptors gate the release of glutamate onto postsynaptic neurons. Photoreceptor synapses are specialized with a vesicle-associated ribbon organelle and postsynaptic neurites of horizontal and bipolar cells that invaginate deep within the terminal [1]. A variety of proteins interact with the ribbon and synaptic vesicles near release sites (*i.e.,* active zones) [2]. The importance of these proteins for vision is illustrated by the numerous inherited retinal diseases linked to mutations in their encoding genes [3].

One such gene is *CACNA1F*, which encodes the voltage-gated Ca^{2+} (Ca_v) channel expressed in retinal photoreceptors, $Ca_v1.4$ [4-6]. Among the sub-family of Ca_v1 L-type channels, $Ca_v1.4$ exhibits unusually slow inactivation that is well-matched for supporting the tonic, Ca^{2+}-dependent release of glutamate from photoreceptor synaptic terminals in darkness [7, 8]. More than 200 mutations in *CACNA1F* cause vision disorders including congenital stationary night blindness type 2 (CSNB2) [9, 10]. These mutations are broadly categorized as producing a gain of function or loss of function in $Ca_v1.4$ [11]. How these mutations in *CACNA1F* lead to the variable clinical phenotypes of CSNB2 is largely unknown. Symptoms may include strabismus, low visual acuity, and in many cases, night blindness [12, 13]. The latter suggests a primary defect in rod pathways, which is surprising given that $Ca_v1.4$ knockout (KO) mice are completely blind and lack any evidence of either rod or cone synaptic responses [4, 5, 14]. A major caveat is that rod and cone synapses do not form in $Ca_v1.4$ KO mice [5, 14-16]. Thus, $Ca_v1.4$ KO mice are not suitable for studies of how *CACNA1F* mutations differentially affect rod and cone pathways or for efforts to uncover how the biophysical properties of $Ca_v1.4$ shape photoreceptor synaptic release properties.

Here, we overcome this hurdle with a knock-in mouse strain (G369i KI) expressing a non-conducting mutant form of $Ca_v1.4$ [17]. We show that, although greatly impaired, cone synapses and downstream signaling through cone pathways can support photopic visual function in G369i KI mice. This novel mechanism requires the ability of the $Ca_v1.4$ protein, independent of its Ca^{2+} conductance, to nucleate the assembly of cone ribbon synapses and involves an aberrant Ca_v3 (T-type) conductance that appears when $Ca_v1.4$ Ca^{2+} signals are compromised.

RESULTS

Cone pedicles and ribbons are present in G369i KI mice but not in $Ca_v1.4$ KO mice

The G369i mutation results in an insertion of a glycine residue in a transmembrane domain, which prevents Ca^{2+} permeation through $Ca_v1.4$[17]. The presence of rod synapses in G369i KI mice but not $Ca_v1.4$ KO mice indicates that the $Ca_v1.4$ protein and not its Ca^{2+} conductance is required for rod synapse assembly[17]. To test if this is also true for cones, we performed immunofluorescence and confocal analyses using antibodies against cone arrestin (CAR) and CtBP2 to label cone terminals (i.e., pedicles) and ribbons, respectively (Fig. 1). In $Ca_v1.4$ KO mouse retinas, cone pedicles were shrunken and retracted into the outer nuclear layer (ONL, Fig. 1a) with little evidence of elongated ribbons (Fig. 1b). In contrast, cone pedicles in G369i KI mice were normally localized in the outer plexiform layer (OPL, Fig. 1a) and were populated by multiple ribbons that were associated with labeling for $Ca_v1.4$ (Fig. 1b). Some abnormalities were apparent in G369i KI cone pedicles, such as extremely elongated ribbons and telodendria extending towards the inner nuclear layer (Fig.1b). These results indicate that $Ca_v1.4$ Ca^{2+} signals are dispensable for the integrity of ribbons and the pedicle but are necessary for their overall refinement.

Ca_v3 channel activity is present in cones of G369i KI and $Ca_v1.4$ KO mice but not WT mice, ground squirrel, or macaque retina

A prevailing yet unsupported hypothesis regarding the relatively mild visual phenotypes in CSNB2 is that additional Ca_v subtypes may compensate for $Ca_v1.4$ loss-of-function in cones. If so, then Ca^{2+} currents (I_{Ca}) mediated by these subtypes should be evident in cones of $Ca_v1.4$ KO and G369i KI mice. To test this, we performed patch clamp recordings of cones in retinal slices of adult WT, G369i KI, and $Ca_v1.4$ KO mice under conditions designed to isolate I_{Ca}. During voltage ramps in WT cones, I_{Ca} activated around -50 mV and peaked near -20 mV, consistent with the properties of $Ca_v1.4$ (Fig. 2a-d). While not observed in rods of G369i KI or $Ca_v1.4$ KO mice[17], a small-amplitude I_{Ca} that activated around -60 mV and peaked near -35 mV was detected in cones of these mice (Fig.2a-d). To uncover this low voltage-activated I_{Ca}, we

used a faster voltage ramp (0.5 mV/ms) than in the previous study of G369i KI rods (~0.15 mV/ms)[17]. With this faster voltage ramp, I_{Ca} was not apparent in G369i KI rods (Fig.2 Fig.Supp. 1). Therefore, the aberrant I_{Ca} is an adaptation to $Ca_v1.4$ loss-of-function in cones but not rods.

We next used step depolarizations to identify the type of Ca_v channel underlying I_{Ca} in G369i KI and $Ca_v1.4$ KO cones. Analysis of current-voltage (I-V) and conductance-voltage (G-V) relationships revealed a significant, hyperpolarizing shift (~10 mV) in the voltage of half maximal activation (V_h) in G369i KI cones (Fig.2c,d; Table 1). I_{Ca} in G369i KI cones was not sustained as in WT cones but inactivated rapidly during 500-ms step depolarizations (Fig. 2e). For G369i KI cones, overlay of the conductance-voltage (Fig. 2d) and inactivation curves revealed a sizeable window current (Fig. 2f). These features of I_{Ca} in G369i KI and $Ca_v1.4$ KO cones resembled those of Ca_v3 T-type channels rather than $Ca_v1.4$[18].

In a previous study, a Ca_v3-like current was detected in patch clamp recordings of cone pedicles in WT mouse cones[19]. However, in recordings of WT mouse cone somas, we did not observe a low-voltage activated component in the I-V or G-V curves that would be indicative of a Ca_v3 subtype (Fig.2c,d). To further test for a Ca_v3 contribution to I_{Ca} in WT mouse cones, we used a double pulse voltage protocol where I_{Ca} was evoked before (P1) and after (P2) a 500-ms step to -60 mV (Fig.2g). With this protocol, the inactivation of Ca_v3 channels by the -60 mV step should lead to a reduction in the amplitude of the P2 vs the P1 current. While such a reduction was clearly evident in cones of G369i KI mice (i.e., P2/P1 < 1), there was no significant difference in the P2 and P1 currents in cones of WT mice (Fig.2g-i).

We also used antagonists selective for Ca_v1 and Ca_v3 channels (isradipine and ML 218, respectively). As expected, I_{Ca} in WT cones was significantly but incompletely suppressed by isradipine (Fig. 3a,b). The V_h of the I-V was similar before (-36.5 $\pm$ 0.8 mV) and after (-38.3 $\pm$ 1.8 mV) perfusion of isradipine ($t(3,4)=0.90$, $p = 0.43$ by paired t-test), suggesting that the residual I_{Ca} after exposure to isradipine arose from unblocked $Ca_v1.4$ rather than Ca_v3 channels. While ML 218 modestly inhibited I_{Ca} in some WT cones, the effect was not statistically significant (Fig.

3c,d) and could be attributed to weak activity on $Ca_v1.4$. In transfected HEK293T cells, ML 218 modestly inhibited I_{Ca} and caused a negative shift in the V_h for $Ca_v1.4$, in contrast to its strong inhibition of $Ca_v3.2$ (Fig.3-Fig.Supp.2). Like its effects on $Ca_v3.2$, ML 218 nearly abolished I_{Ca} in cones of G369i KI mice whereas isradipine had little effect (Fig. 3a-d).

Finally, we recorded from ground squirrel and macaque cones, where the large amplitude of I_{Ca} facilitates pharmacological and biophysical analyses. Consistent with its actions on $Ca_v1.4$ in WT mouse cones (Fig. 3b) and transfected HEK293T cells (Fig.3-Fig.Supp.2), ML 218 caused an insignificant inhibition of peak I_{Ca} (-7.0 ± 20.8%, n = 6 cones) as well as a negative shift in the voltage-dependence of activation in ground squirrel cones ($\Delta V_{1/2}$ = -1.16 ± 0.94 mV, n = 6, mean ± SD, p = 0.029, t-test; Fig. 4a,b). By contrast, application of isradipine dramatically suppressed I_{Ca} in cones in various regions of the ground squirrel retina (Fig. 4c,d). Subsequent application of ML 218 did not reveal a Ca_v3-like current: the I-V and G-V of the isradipine + ML 218-sensitive current were shifted in the positive rather than the negative direction relative to the isradipine-sensitive current (Fig.4c-g). This result is consistent with the time- and voltage-dependent block of Ca_v1 channels by dihydropyridine antagonists such as isradipine [20]. As a positive control, we confirmed that ML 218 blocked a prominent Ca_v3-type current in ground squirrel type 3a OFF cone bipolar cells (Fig.4h,i). In recordings of macaque cone pedicles, we compared the properties of I_{Ca} using a holding voltage of -90 mV or -50 mV, the latter of which should inactivate Ca_v3 channels (Fig.5a). There was no difference in the I-V or G-V relationships obtained at these holding voltages (Fig.5b-e). As in WT mouse cones (Fig.2g-i), there was also no difference in I_{Ca} recorded before and after an inactivating pulse to -60 mV (Fig.5f,g). We conclude that Ca_v3 channels do not normally contribute to I_{Ca} in cones of WT mice, ground squirrel, and macaque.

To test whether the appearance of the Ca_v3-mediated I_{Ca} in G369i KI cones could result from an increase in the expression of a specific Ca_v3 subtype (*i.e.,* $Ca_v3.1$, $Ca_v3.2$, or $Ca_v3.3$), we initially tried labeling with commercially available antibodies against $Ca_v3.2$. However, the

data were unreliable since these antibodies produced a similar labeling pattern in $Ca_v3.2$ KO retinal tissue (data not shown). As an alternative, we performed single cell RNA sequencing on cells isolated from the retina of WT and G369i KI mice (Fig.2-Fig.Supp.3). We sequenced 28,782 cells and, with unsupervised clustering at resolution=0.5, we grouped the cells into 20 clusters. Clusters 8 and 16 were identified as cones based on the expression of cone marker genes (e.g., Opn1sw, Opn1mw, Arr3, Gnat2). Consistent with previous studies[19, 21], *Cacna1h* encoding the $Ca_v3.2$ subtype was the major Ca_v3 transcript expressed in WT mouse cones. There was no significant difference in *Cacna1h* expression between WT and G369i KI cones according to this analysis (Fig.2-Fig.Supp.3). Thus, the enhanced activity of Ca_v3 channels in cones of G369i KI mice results from a mechanism other than increased transcription of *Cacna1h*.

Cone synapses are enlarged with some errors in postsynaptic wiring in G369i KI mice

The replacement of $Ca_v1.4$ with Ca_v3 as the primary conduit for Ca^{2+} influx in G369i KI cones allowed us to dissect the importance of $Ca_v1.4$ Ca^{2+} signals for the molecular and structural organization of the cone synapse. To this end, we first analyzed WT and G369i KI cone synapses by immunofluorescence and confocal microscopy. Presynaptic proteins such as bassoon and members of the postsynaptic signaling complex in depolarizing (ON) cone bipolar cells (GPR179, mGluR6, and TRPM1[22]) were enriched near cone ribbons in G369i KI mice as in WT mice (Fig. 6a). Compared to WT mice, the labeled structures in G369i KI mice occupied a larger volume (Fig. 6b,c) but were of lower intensity (Fig. 6d), suggesting an increase in the spread rather than in the levels of synaptic proteins. Unlike in WT mice, the volume of presynaptic and postsynaptic proteins increased linearly with the volume of the pedicle in G369i KI mice (Fig. 6e-i). These results show that the molecular determinants of the cone synapse can assemble in G369i KI mice but change in their sub-synaptic distribution in ways that correlate with the expansion of the cone pedicle.

The cone synapse is structurally complex, with the dendritic tips of two horizontal cells and an intervening ON cone bipolar cell invaginating deeply into the pedicle near the ribbon [1]. To test how the switch in Ca_v subtypes might affect this arrangement of postsynaptic partners, we generated 3D reconstructions of cone synapses by serial block-face scanning electron microscopy (SBFSEM; Fig. 7). As with the enlarged synaptic contacts (Fig. 6), structural modifications in G369i KI pedicles were evident. Compared to WT, ribbons in G369i KI pedicles appeared disorganized and were often parallel rather than perpendicular to the presynaptic membrane (Fig.7a-c). Consistent with our confocal analyses (Fig.1), G369i KI cone pedicles extended telodendria in multiple directions rather than just apically (Fig. 7a). In addition, a slightly larger fraction of synaptic sites in the G369i KI pedicle (35% vs 14% in WT) formed incorrect postsynaptic partnerships including with glia (Fig.7b-d'; Table 2). Nevertheless, the number of ribbons is normal in G369i KI cones and about half of the ribbons make invaginating contacts with the appropriate cell types (*i.e.,* both horizontal cells and cone bipolar cells; Table 2). On average, there were more vesicles associated with ribbons in cones of G369i KI mice (245 per ribbon) than of WT mice (178 per ribbon; Table 2), but the difference did not reach statistical significance. Together with our immunofluorescence data, these results indicate that cone synapses undergo relatively subtle morphological changes in G369i KI mice, perhaps in response to the loss of $Ca_v1.4$ Ca^{2+} signals.

Postsynaptic responses to light are present in horizontal cells of G369i KI mice but not $Ca_v1.4$ KO mice

Compared to $Ca_v1.4$ KO mice, the relative preservation of cone synapses in G369i KI mice allowed the unique opportunity to test whether a Ca_v subtype other than $Ca_v1.4$ could support synaptic release. To this end, we analyzed synaptic transmission between cones and horizontal cells (HCs). In darkness, glutamate released from cones depolarizes horizontal cells via activation of α-amino-3-hydroxy-5-methyl-4-isoxazolepropionic (AMPA)/kainate receptors[23,

[24]. The resulting excitatory postsynaptic current (EPSC) undergoes a decline in response to light stimuli that hyperpolarize cones[25]. In WT HCs, a 1-s light flash (λ=410 nm) inhibited the standing EPSC, which is reflected as an outward (hyperpolarizing "ON") current (Fig. 8a). Upon termination of the light, an inward (depolarizing "OFF") current signaled the resumption of the EPSC (Fig. 8a). Both the ON and OFF responses in WT HCs increased with light intensity, reflecting the impact of luminance on the presynaptic membrane potential of cones and the subsequent change in glutamate release from their terminals (Fig. 8b).

Consistent with the lack of mature ribbons and abnormal cone pedicles (Fig.1), HC light responses were negligible in $Ca_v1.4$ KO mice (Fig.8a,b). In contrast, the ON and OFF responses were present in G369i KI HCs although significantly lower in amplitude than in WT HCs (Fig. 8a,b). As expected, the EPSC in darkness and the light responses were abolished by the AMPA/kainate receptor antagonist, DNQX, in both WT and G369i KI HCs (Fig. 8c,d). In addition to its smaller amplitude, the transient nature of the ON response in G369i KI HCs suggested inadequate cessation of cone glutamate release by light (Fig.8b). Slow deactivation of Ca_v3 channels and/or their activation at negative voltages[18] could give rise to Ca^{2+} signals that support release following light-induced hyperpolarization of G369i KI cones.

To test if the diminished HC light responses correlated with lower presynaptic Ca^{2+} signals in G369i KI cones, we performed 2-photon imaging of vertical slices prepared from whole retina that was incubated with the Ca^{2+} indicator Fluo3-AM and Alexa-568-conjugated peanut agglutinin (PNA) to demarcate regions of interest (ROIs) corresponding to cone pedicles. With this approach Fluo3 fluorescence was detected only in photoreceptors and ganglion cells and not inner retinal cell-types (e.g., horizontal cells, bipolar cells, Mueller cell soma). Thus, Ca^{2+} signals reported by Fluo3 fluorescence near PNA-labeling originated primarily from cones. In WT cones, depolarization by K^+ (50 mM) caused a sustained increase of Ca^{2+} ($\Delta F/F_0$ = 1.85 ± 0.1, n = 11 terminals) that was significantly lower after the addition of isradipine ($\Delta F/F_0$ = 1.44 ± 0.07, p = 0.0015 by repeated measures one-way ANOVA with

Tukey's multiple comparison posthoc test; F[1.608, 16.08] = 55.17; $p < 0.0001$; Fig.9a,b). The Ca^{2+} signal remaining in the presence of isradipine could arise from unblocked $Ca_v1.4$ channels and/or Ca^{2+} release from intracellular stores[26]. In G369i KI cones, the peak amplitude of the K^+-evoked Ca^{2+} signal ($\Delta F/F_0$ = 1.07 ± 0.02, n = 14 terminals) was significantly lower than in WT cones (t(23)=8.74, $p < 0.0001$ by unpaired t-test, n = 14 terminals). The decrease in the Ca^{2+} signal in the G369i KI cone pedicles during isradipine exposure paralleled that during the depolarization (Fig.9a), suggesting it was not a consequence of Ca_v1 blockade. The lower amplitude and more transient Ca^{2+} signals mediated by Ca_v3 channels may be cleared more rapidly in G369i KI cones as compared to prolonged $Ca_v1.4$-initiated Ca^{2+} signals in WT cones. Taken together, our results suggest that Ca_v3 channels nominally support Ca^{2+} signals and synaptic transmission in cones of G369i KI mice.

Light responses of bipolar cells and visual behavior are present in G369i KI but not $Ca_v1.4$ KO mice

While HCs play important roles in lateral inhibition of photoreceptor output, the vertical dissemination of visual information from cones to the inner retina is relayed by glutamate to ON and OFF cone bipolar cells (CBCs) which express mGluR6 and AMPA/kainate receptors, respectively. To test for the existence of cone to CBC transmission in G369i KI mice, we recorded electroretinograms (ERGs) under light-adapted conditions using $Ca_v1.4$ KO mice as a negative control (Fig. 10a-d). In these recordings, the light-induced response of photoreceptors and the postsynaptic response of ON CBCs corresponds to the a- and b-waves, respectively. Unlike in $Ca_v1.4$ KO mice, the a-waves of G369i KI mice resembled those in WT mice, which indicates that cones do not degenerate in this mouse strain (Fig. 10a,b). While greatly reduced in amplitude, the b-wave was measurable in G369i KI mice and significantly larger than in $Ca_v1.4$ KO mice at the highest light intensities ($F(14,104)=41$, $p<0.0001$, post-hoc Tukey's $p=0.0038$ at 2.3 log cd·s/m^2; Fig. 10a,b). We also recorded flicker ERGs using 10 Hz light

stimuli that can isolate cone pathways involving both ON and OFF CBCs[27, 28]. In WT mice, flicker responses exhibited two peaks, one at a lower irradiance (-2 log cd·s/m^2) and one at higher irradiance (0.5 log cd·s/m^2; Fig.10c,d). The peak at the lower irradiance is attributed to responses in both rod and cone pathways, and the peak at higher irradiance is attributed to responses exclusively in cone pathways[27, 28]. Flicker responses in G369i KI mice showed a similar non-monotonic relation as in WT mice but were significantly lower in amplitude ($F(26,143)=51.18$, $p<0.0001$, post-hoc Tukey's $p=0.0237$ at 2.5 log cd·s/m^2; Fig.10c,d). The inverted flicker responses at higher illuminations in G369i KI mice were absent in $Ca_v1.4$ KO mice and may result from the hyperpolarizing contribution of cone-to-OFF CBC transmission (Fig.10c).

To test whether the cone synaptic responses in G369i KI mice enable vision-guided behavior, we used a swim test that assesses the ability of mice to identify a visible platform[29]. Under scotopic (dark) conditions, G369i KI and $Ca_v1.4$ KO mice took significantly longer to find the platform compared to WT mice (Fig. 10e,f). These results are consistent with flicker response assays (Fig.10c,d) as well as the absence of I_{Ca} in rods and rod-to-rod bipolar cell synaptic transmission in G369i KI mice[17]. Under photopic (light) conditions, G369i KI mice but not $Ca_v1.4$ KO mice performed as well as WT mice (Fig. 10e,f). Thus, G369i KI mice have enough visual function under photopic conditions to quickly find the platform. Collectively, our results suggest that Ca_v3 channels can support cone synaptic responses that are sufficient for visual behavior in G369i KI but not $Ca_v1.4$ KO mice.

DISCUSSION

The nervous system has remarkable abilities to adapt to pathological perturbations in neuronal activity. In the retina, ablation or degeneration of photoreceptors triggers various postsynaptic mechanisms that maintain some level of visual function in rod or cone pathways. These include remodeling of bipolar cell dendrites and their synapses[30-32] as well as changes in

the sensitivity of bipolar cells to photoreceptor input and inhibitory modulation[32, 33]. To our knowledge, this study provides the first evidence for a presynaptic form of homeostatic plasticity that originates within photoreceptors. Using $Ca_v1.4$ KO and G369i KI mice, we identify the upregulation of a Ca_v3 conductance as a common response to $Ca_v1.4$ loss-of-function in cones. However, Ca_v3 channels can only compensate for $Ca_v1.4$ loss-of-function if the basic aspects of cone synapse structure are maintained through expression of the G369i mutant channel. Thus, our results also highlight a crucial, non-conducting role for the $Ca_v1.4$ protein that allows cone synapses to function in the absence of $Ca_v1.4$ Ca^{2+} signals.

A non-canonical role for $Ca_v1.4$ in regulating cone synapse assembly

As shown for rod synapses[17], ribbons and other components of the pre- and post-synaptic complex assemble at cone synapses in G369i KI mice (Figs. 1,6,7). Ca_v3 Ca^{2+} signals are dispensable for this process since their presence in $Ca_v1.4$ KO cones is not accompanied by any semblance of ribbon synapses (Fig.1b). An intimate relationship between $Ca_v1.4$ and ribbons is supported by the colocalization of $Ca_v1.4$ and puncta resembling ribbon precursor spheres in the developing OPL[5]. $Ca_v1.4$ interacts directly or indirectly with a variety of ribbon synapse associated proteins including RIM [34], CAST/ERC2 [35], bassoon[36], unc119[37-39], and a major component of the ribbon, RIBEYE[40]. $Ca_v1.4$ could pioneer sites of ribbon assembly perhaps by serving as a docking or nucleation site for the active zone. At the same time, ribbon-associated proteins help cluster $Ca_v1.4$ near ribbons since knockout of these proteins in mice leads to fewer presynaptic $Ca_v1.4$ channels and in some cases shortened ribbons[41]. Regardless of the mechanism, our findings show that the formation of photoreceptor synaptic complexes does not require Ca^{2+} influx through $Ca_v1.4$ channels.

Functional Ca_v3 channels are present in cones in the absence of $Ca_v1.4$ Ca^{2+} signals

Our drop-seq analysis aligns with previous studies indicating that *Cacna1h* is expressed at extremely low levels compared to *Cacna1f* in WT mouse cones (Supp.Fig.S3)[21, 42]. However, in contrast to recordings of WT mouse cone pedicles in a previous study[19], we found no evidence for Ca_v3-mediated currents in somatic recordings of cones in WT mice (Figs.2,3). We do not feel the discrepancy results from the different recording configurations given the electrically compact nature of cones. Moreover, recordings from macaque cone pedicles and from the ellipsoids of cylindrically-shaped ground squirrel cones also did not reveal a Ca_v3-mediated current (Figs.4,5). We acknowledge that there are caveats of the pharmacological approach used in our study as well as the previous work[19]. For example, dihydropyridine antagonists such as isradipine have relatively low affinity for some Ca_v1 subtypes, including $Ca_v1.4$[20, 43] and have strongly voltage-dependent blocking properties. At a holding voltage of -90 mV, isradipine at 1 μM causes only ~80% inhibition of $Ca_v1.4$ with greater block at depolarized voltages[20], which agrees with our recordings of cones in WT mice (Fig.3a) and ground squirrels (Fig.4b-e). Moreover, in the low micromolar range, Ca_v3 blockers such as Z944 [44] and ML 218 (Supp.Fig. S2) have nonspecific effects on Ca_v1 current amplitude and activation voltage. Thus, Ca_v channels mediating a I_{Ca} that is suppressed by Ca_v3 blockers and spared by dihydropyridines at negative voltages may be mistakenly categorized as Ca_v3 subtypes. In our experiments, the biophysical properties of the isradipine-sensitive I_{Ca} in cones of WT mice and ground squirrels resembled only those of Ca_v1, whereas those of the ML 218-sensitive I_{Ca} in cones of G369i KI mice resembled only those of Ca_v3. Therefore, we favor the interpretation that Ca_v3 contributes to I_{Ca} in mouse cones only upon silencing of $Ca_v1.4$ either by KO of the corresponding protein or by silencing its conductance.

Since *Cacna1h* expression was similar in WT and G369i KI cones (Supp.Fig.S3), what causes the increased Ca_v3 channel activity in the latter? Among the Ca_v3 subtypes, $Ca_v3.2$ is uniquely sensitive to post-translational modifications that facilitate the opening of the channel and/or its cell surface trafficking[45]. For example, $Ca_v3.2$ interacts with the deubiquitinating

enzyme USP5 which enhances levels of $Ca_v3.2$ protein levels by suppressing its proteasomal degradation[46]. In addition, $Ca_v3.2$ is phosphorylated by calmodulin-dependent kinase II[47] and cyclin-dependent kinase 5[48], which enhances channel activation and current density, respectively. Further interrogation of our drop-seq dataset could illuminate novel $Ca_v3.2$-regulatory pathways that are modified in G369i KI cones.

Consequences of $Ca_v1.4$ loss of function and relevance for CSNB2

Despite having the same complement of proteins as in WT mice, cone synapses in G369i KI mice were enlarged and made errors in postsynaptic partner selection (Figs.6,7). While I-V curves indicate similar peak I_{Ca} amplitudes in cones of WT and G369i KI mice near the membrane potential of cones in darkness (-45 to -50 mV[49], Fig.2a,c), the strong inactivation of Ca_v3 channels and/or reduced Ca^{2+} release from intracellular stores likely account for the greatly diminished Ca^{2+} signals in G369i KI pedicles (Fig.9). Paradoxically, reductions in presynaptic Ca^{2+} in rod photoreceptors correlated with illumination-dependent shrinkage of ribbons *in vivo* and *in vitro*[50-52]. However, ribbon synapse size increases with low presynaptic Ca^{2+} in zebrafish sensory hair cells[53]. The mechanism involves decreased mitochondrial Ca^{2+} uptake and increase in the redox state of nicotinamide adenine dinucleotide (NAD^+/NADH ratio) [54]. Ca_v3 Ca^{2+} signals may decay too quickly in G369i KI cones (Fig.9) to enable mitochondrial Ca^{2+} uptake or other mechanisms that trim ribbons.

An intriguing result was the linear increase in ribbon synapse size with pedicle volume in G369i KI but not in WT mice (Fig. 6e-i), which could represent a form of homeostatic synaptic scaling as has been demonstrated at the neuromuscular junction[55, 56]. Similarly, the presence of some non-invaginating contacts with incorrect partner pairings in G369i KI mice (Fig.7, Table 2) could be an attempt to increase synaptic connectivity to compensate for weakened synaptic

output. Consistent with this possibility, diminished presynaptic Ca^{2+} signals and non-invaginating cone synapses also characterize the retina of mice lacking the extracellular $\alpha_2\delta$–4 subunit of $Ca_v1.4$[57]. The cone synapses of G369i KI mice and $\alpha_2\delta$–4 KO mice are clearly functional given that photopic visual behavior is preserved in both mouse strains (Fig.10e,f)[57] and, in the case of G369i KI mice, HCs exhibit EPSCs whose amplitude decreases with light and AMPA/kainate receptor blockade (Fig.8). Defects in cone synaptic transmission that correlate with aberrant cone synapse morphology and connectivity also typify a mouse strain with a gain-of function mutation in $Ca_v1.4$ linked to CSNB2[58, 59]. Thus, balanced presynaptic Ca^{2+} signals may be needed to encode the correct post-synaptic wiring and structure of the cone synapse.

In addition to structural abnormalities in cone synapses, the inability of Ca_v3 channels to support sustained presynaptic Ca^{2+} entry likely contributed to the impaired light responses in HCs and CBCs in G369i KI mice (Figs.8,10). Due to their slow activation and strong inactivation [60], Ca_v3 channels are not expected to fuel the Ca^{2+} nanodomains that support fast and sustained components of release, both of which occur only at ribbon sites in cones[61 62]. Ca_v3 channels may also be located further from the ribbon than $Ca_v1.4$, thus lowering the efficiency of coupling to exocytosis. Regardless of the features that differentiate the contributions of Ca_v3 and $Ca_v1.4$ to cone synaptic release, our findings provide further support for the widely held view that Ca_v1 channels are well-suited to support transmission at ribbon-type synapses.

Based on extremely heterogeneous clinical presentations, CSNB2 manifests as a spectrum of visual disorders that originate from various mutations in *CACNA1F* [12, 63]. Even though some CSNB2 mutant $Ca_v1.4$ channels may traffic normally to the plasma membrane, many of these mutations are expected to produce non-functional, non-conducting $Ca_v1.4$ channels[64, 65]. Yet, the visual phenotypes of CSNB2 patients are not as severe as the complete blindness in $Ca_v1.4$ KO mice, which lack any $Ca_v1.4$ protein expression and exhibit no signs of visual behavior (Fig.10e,f)[57]. Collectively, our results suggest that G369i KI mice accurately

model $Ca_v1.4$ channelopathies in CSNB2 patients that are characterized by a greater impairment in rod than in cone pathways. This interpretation is supported by our findings that G369i KI mice exhibit horizontal cell responses to bright but not dim illumination (Fig. 8), ERG responses under conditions of light adaptation (Fig.10a-d) but not dark-adaptation [17], and visual behavior under photopic but not scotopic conditions (Fig. 10e,f). Together with the enlargement of synaptic sites, modest levels of synaptic release from cones of G369i KI mice may support nominal transmission of visual information through cone pathways. G369i KI mice could also exhibit homeostatic alterations in the inner retina, which are known to support visual function when photoreceptor input is severely compromised [31-33]. Future studies of the retinal circuitry and visual behavior of G369i KI mice could identify compensatory pathways that are recruited upon $Ca_v1.4$ loss-of-function and how they might be targeted in novel therapies for CSNB2 and related disorders.

ACKNOWLEDGEMENTS

J.W.M., G.J.O., J.D.V., A.H., K.R., and A.L. were supported by NIH grants EY026817 (to A.L.), EY029953 (to J.W.M.), and unrestricted funds from the University of Texas-Austin (to A.L.); S.R.W. and M.H. were supported by NIH grant EY031677 (to M.H.), an unrestricted grant from RPB to UW Madison Dept. of Ophthalmology and a McPherson ERI professorship to M.H.; D.F. and S.H.D. were supported by NIH grants EY012141 and EY032506, an unrestricted grant from RPB to the Northwestern University Dept. of Ophthalmology, and an RPB International Travel Award. N.A.S. and R.D. Mayfield were supported by AA029955 (N.A.S) and AA0012404 and AA020926 (R.D.M.). The authors thank J. Sun for assistance with acquiring some of the electrophysiological data in Supp.Fig.S2, S. Knecht and R. Wong for assistance with serial EM image collection, E. Seidemann and B. Shukla for the generous donation and collection of macaque retinal tissue, respectively, and M. McCall and F. Vinberg for advice on ERGs.

AUTHOR CONTRIBUTIONS

Conceptualization, J.W.M., G.O., A.L.; Methodology, J.W.M., G.O., J.D.V., A.L., M.H., S.H.D., D.F., N.S., R.D.M; Investigation, J.W.M., G.O., J.D.V., A.H., C.G., K.R., S.R.W., S.H.D., D.F.; Writing—original draft, A.L.; Writing—review and editing, J.W.M., G.J.O., M.H., S.H.D., A.L.; N.S., R.D.M. Funding acquisition, J.W.M., M.H., S.H.D., A.L., R.D.M.

DECLARATION OF INTERESTS

The authors declare no competing interests.

Table 1. Comparison of parameters from electrophysiological recordings of cones.

	C_M (pF)	P-value	n	R_M (MΩ)	P-value	n
WT	4.88 (3.86, 5.01)	--	11	3.57 (2.81, 4.65)	--	11
G369i KI	4.08 (3.88, 4.34)	0.73[a]	9	5.06 (4.04, 8.24)	0.04[a]	9
$Ca_v1.4$ KO	3.31 (3.00, 3.76)	0.001[a], 0.04[b]	6	8.21 (7.26, 9.06)	0.001[a], 0.47[b]	6
G-V	V_h (mV)	P-value	n	k	P-value	n
WT	-37.54 (-38.91, -35.13	--	13	2.75 (2.47, 4.32)		13
G369i KI	-47.59 (-50.07, -46.72)	0.0001[a]	9	2.99 (2.68, 4.16)	0.99[a]	9
$Ca_v1.4$ KO	-44.98 (-50.15, -43.27)	0.085[a], 0.99[b]	3	4.33 (3.73, 5.22)	0.34[a], 0.49[b]	3
Steady state inactivation	V_h (mV)	P-value	n	k	P-value	n
WT	-49.06 (-57.95, -41.82)	--	8	-7.25 (-12.30, -4.97)	--	8
G369i KI	-59.40 (-62.73, -58.01)	0.01[a]	8	-3.81 (-5.23, -2.46)	0.12[a]	8
$Ca_v1.4$ KO	-56.62 (-61.65, -56.56)	0.88[a], 0.88[b]	3	-3.67 (-5.17, -1.19)	0.14[a], 0.99[b]	3
	Tau activation	P-value	n	Tau deactivation	P-value	n
WT	2.04 (1.26, 2.71)	--	11	0.88 (0.62. 2.09)	--	6
G369i KI	3.32 (2.99, 4.06)	0.001[a]	9	3.40 (2.62, 4.34)	0.004[a]	6

Values represent median (25th, 75th quartiles). V_h and k were determined from Boltzmann fits of the G-V and steady-state inactivation curves. Time constant (tau) for activation was obtained from exponential fit of the rising phase of I_{Ca} evoked by a 50-ms test pulse to a voltage near the peak of the I-V. Tau deactivation was determined from exponential fit of the decay of the tail current evoked by repolarization to -90 mV from +20 mV. C_M, membrane capacitance; R_M, input

resistance. P-values were determined by Kruskal Wallis test. [a], relative to WT. [b], relative to G369i KI.

Table 2. Comparison of parameters for cone synapse organization

	WT		G369i KI	
	Cone 1	Cone 2	Cone 1	Cone 2
# of ribbons	12	8	8	6
Mean # synaptic vesicles per ribbon	137.75	218.25	224	267.5
Type of contact: % total (fraction of total)				
Invaginating	58.3 (7/12)	87.5 (7/8)	50 (4/8)	50 (3/6)
Non-invaginating	41.7 (5/12)	12.5 (1/8)	50 (4/8)	50 (3/6)
Partner composition: % total (fraction of total)				
HC/BC	83.3	87.5	50.0	66.7
HC only	8.3	12.5	25.0	33.3
BC only	8.3	0	12.5	0
Glia only	0	0	12.5	0

Results represent analysis of n = 2 pedicles reconstructed by serial block face scanning electron microscopy in images obtained from WT or G369i KI mice (N= 1 animal each). The first row of vesicles encircling and immediately apposed to the ribbon were quantified for all the z-planes of the ribbon. Sites were counted as 'invaginating' if postsynaptic partners were enveloped on all sides by the cone terminal for at least a couple of consecutive image planes.

FIGURE LEGENDS

Figure 1. Cone pedicles and the mutant $Ca_v1.4$ G369i channel are normally localized in the retina of G369i KI mice but not $Ca_v1.4$ KO mice. Confocal images of the outer nuclear layer (ONL) and outer plexiform layer (OPL) of retina from WT, G369i KI, and $Ca_v1.4$ KO mice that were labeled with antibodies against cone arrestin (CAR), CtBP2, and $Ca_v1.4$. ***a***, Inverted images of CAR labeling. Lower panels depict pedicles labeled by CAR antibodies (dotted outlines) and correspond to the boxed regions in the upper panels. Cone pedicles remain in the OPL of WT and G369i KI retina (arrows) but are misshapen and retracted into the ONL of the $Ca_V1.4$ KO retina (open arrowheads). Solid arrowheads indicate telodendria which extend only apically in WT retina but extend basally and laterally in G369i KI retina. ***b***, Deconvolved confocal images showing $Ca_V1.4$ labeling near cone ribbons in WT and G369i KI pedicles (arrows) and ribbon spheres without $Ca_V1.4$ labeling in the $Ca_V1.4$ KO pedicle (arrowheads). Rod-associated CtBP2 and $Ca_v1.4$ labeling was removed for clarity.

Figure 2. A low-voltage activated I_{Ca} is present in cones of G369i KI and $Ca_V1.4$ KO but absent in cones of WT mice. *a*, Representative traces of I_{Ca} evoked by voltage ramps. ***b,*** I_{Ca} traces from *a* normalized to their peak current amplitude to illustrate the hyperpolarizing shift in the I-V from cones of G369i KI and $Ca_V1.4$ KO mice. ***c,d***, I-V (*c*) and G-V (*d*) relationships for I_{Ca} evoked by 50 ms, +5 mV increments from a holding voltage of -90 mV. V_m, test voltage. WT, n = 13; G369i KI, n = 9; $Ca_V1.4$ KO, n = 3. ***e*,** Representative I_{Ca} traces and voltage protocol (bottom) for steady-state inactivation. I_{Ca} was evoked by a conditioning pre-pulse from -90 mV to various voltages for 500 ms followed by a test pulse to -30 mV for 50 ms. ***f***, Steady-state inactivation data from cones as recorded in *e*. I/I_{max} represents the current amplitude of each -30-mV test pulse (I) normalized to current amplitude of the -30-mV test pulse preceded by a -90 mV conditioning pre-pulse (I_{max}) and was plotted against pre-pulse voltage. Shaded region

indicates window current for G369i KI cones. Line without symbols represents G-V curve for G369i KI cones replotted from *d*. WT, n = 8; G369i KI, n = 8; $Ca_v1.4$ KO, n = 3. In graphs *c,d,* and *f,* smooth lines represent Boltzmann fits, symbols and bars represent mean ± SEM, respectively. ***g,*** Representative I_{Ca} traces from WT and G369i KI cones and voltage protocol (top). I_{Ca} was evoked by a step from -100 mV to -30 mV before (P1) or after (P2) a 500 ms step to -60 mV. ***h,i,*** Graphs depicting peak amplitude of I_{Ca} during P1 and P2 steps (*h*) and the ratio of the amplitudes of I_{Ca} evoked by P2 and P1 pulses (P2/P1; *i*) from cones recorded as in *g*. WT, n = 6; G369i KI, n = 6, *p < 0.05 by paired t-test.

Figure 3. Pharmacological characterization of I_{Ca} in cones of WT and G369i KI mice. ***a,*** Representative traces for I_{Ca} evoked by voltage ramps in cones of retinas from WT (top) and G369i KI (bottom) mice before (baseline) and after exposure to isradipine (ISR, 1 μM). Middle panel, WT I_{Ca} from voltage ramps in the top panel were normalized to their peak I_{Ca} to clarify the similar properties of I_{Ca} before and after ISR exposure. ***b,*** Peak I_{Ca} before (-) and during (+) ISR exposure from cones as recorded in *a*. WT, n = 4; G369i KI, n = 5; *p < 0.05 by paired t-test. ***c,*** Representative traces for I_{Ca} evoked by voltage ramps in cones of retinas from WT or G369i KI mice before (baseline) and after exposure to ML 218 (5 μM). Middle panel, WT I_{Ca} from voltage ramps in the top panel were normalized to their peak I_{Ca} to clarify the similar properties of I_{Ca} before and after ML 218 exposure. ***d*,** Peak I_{Ca} before (-) and during (+) ML 218 exposure. WT, n = 5; G369i KI, n = 5; *p < 0.05 by paired t-test.

Figure 4. Pharmacological characterization of I_{Ca} in ground squirrel cones. ***a*,** Representative traces corresponding to baseline-corrected I_{Ca} evoked by voltage ramps before

(baseline) and during application of ML 218. ***b,*** G-V relationship of I_{Ca} in *a*. ***c,*** Representative traces corresponding to I_{Ca} evoked by voltage ramps in control (baseline) and in ISR (2 μM) alone or in ISR+ML 218 (5 μM). ***d,*** Peak I_{Ca} from cones including the record from *c* before (-) and during (+) ISR or ISR+ML 218 block. The changes during the addition of ML218 were small but significant (sup., n = 7, ISR: $p < 0.0001$, ML218: $p = 0.0047$; mid., n = 5, ISR: $p < 0.0001$, ML218: $p = 0.0001$; inf., n = 5, ISR: $p = 0.0019$, ML218: $p = 0.0460$; two-tailed t test) and were likely due to a further non-specific, time-dependent reduction in the Ca_v1 current. ***e,*** I_{Ca} was evoked by steps from -85 mV to voltages between -65 and -5 mV in increments of +10 mV (protocol shown below the current traces in *f*). Representative traces are shown in control, ISR, or ISR+ML 218. Current traces during steps to -55 and -45 mV lacked both transient and ML 218-senstive components. Dashed lines indicate zero current. ***f,*** Traces show the I_{Ca} sensitive to ISR (top) and ISR+ML218 (middle). The I_{Ca} recorded in ISR was subtracted from the baseline I_{Ca} (top). I_{Ca} recorded in ISR+ML218 was subtracted from I_{Ca} recorded in ISR (middle). ***g,*** *Top*, I-V relationship of peak and steady-state I_{Ca} from *f*. *Bottom*, G-V relationship of the I_{Ca} blocked by ISR and ISR + ML218. Smooth lines represent Boltzmann fits. Symbols and bars represent mean ± SEM (n = 4 cones). Due a negative shift in the activation properties caused by ML 218 on a residual Ca_v1 current that is assumed to remain at the end of the experiment, the G-V curve of the I_{Ca} isolated through subtraction by applying ISR+ML 281 underwent a statistically insignificant shift to the right. Data presented in *e-g* are from the same cone. ***h,*** Representative I_{Ca} traces from voltage ramps in an OFF cb3a bipolar cell before and during the application of ML 218. $V_{1/2}$ was shifted to the right by 13.1 ± 4.3 mV (n = 3 cb3a cells, mean ± SD) consistent with the block of a Ca_v3-like conductance. In cb3b OFF bipolar cells, ML 218 produced only a slight leftward shift in an I_{Ca} that had a more depolarized activation range, consistent with the exclusive expression a Ca_v1-type current ($\Delta V_{1/2}$ = -1.9 ± 0.4 mV, n = 3 cells; data not shown). ***i,*** Neurobiotin fill shows cb3a axon stratification and morphology in retina labeled with antibodies

against bassoon and choline acetyltransferase (CHAT) to label the OFF and ON sublamina of the IPL.

Figure 5. Characterization of I_{Ca} in patch clamp recordings of cone pedicles of macaque retina. ***a-c,*** Representative current traces (*a*) and corresponding I-V (*b*) and G-V (*c*) relationships for I_{Ca} evoked by 200-ms steps from a holding voltage of -90 mV or -50 mV. n = 3 cones. ***d,e,*** $V_{1/2}$ (*d*) and slope factor (*e*) obtained from Boltzmann fit of data in *c*. p = 0.50 in *d*; p = 0.25 in *e* by Wilcoxon matched pairs signed rank test. ***f,*** Voltage protocol (*top*) and representative I_{Ca} traces (*bottom left*) from cones as recorded in Fig. 2g-i. Bottom right, expanded view of the boxed region in the left traces. ***g,*** Peak I_{Ca} during P1 and P2 steps from cones recorded as in *f*. n = 5 cones, p = 0.62 by Wilcoxon matched pairs signed rank test.

Figure 6. Immunofluorescence characterization of cone synapses in WT and G369i KI mice. ***a***, Confocal images of the OPL of WT and G369i KI mice labeled with antibodies against cone arrestin (CAR) and proteins that are presynaptic (CtBP2, bassoon) or postsynaptic (GPR179, TRPM1, mGluR6). Every other panel shows high-magnification, deconvolved images of single pedicles labeled with cone arrestin (rod spherule-associated signals were removed for clarity). Arrows indicate ribbon synapses, which appear enlarged in the G369i KI pedicles. ***b***, Violin plot representing volume of presynaptic protein labeling normalized to the volume of their respective CAR-labeled pedicles (volume occupancy). ***c,*** Violin plot representing volume of postsynaptic protein labeling normalized to the volume of their respective CAR-labeled pedicles. ***d,*** Violin plot representing fluorescence intensity of postsynaptic proteins. For *b-d*, **p < 0.01, ***p < 0.001, ****p < 0.0001, unpaired t-tests. ***e-i***, Dependence of synapse size on pedicle size. Volumes corresponding to labeling of CtBP2 (*e*: p = 0.051, r = 0.4 for WT; p < 0.0001, r = 0.88 for G369i KI), $Ca_V1.4$ (*f*: p = 0.8, r = 0.06 for WT; p = 0.002, r = 0.88 for G369i KI), bassoon (*g*: p

= 0.1, r = 0.34 for WT; p < 0.0001, r = 0.75 for G369i KI), mGluR6 (*h*: p = 0.32, r = 0.35 for WT; p = 0.002, r = 0.73 for G369i KI) and TRPM1 (*i*: p = 0.32, r = 0.35 for WT; p = 0.007, r = 0.66 for G369i KI) are plotted against pedicle volume. Dashed and solid lines represent fits by linear regression for WT and G369i KI, respectively.

Figure 7. Three-dimensional reconstruction of cone synapses by SBFSEM. Reconstructions were made of WT and G369i KI pedicles (n = 2 each). ***a***, 3D renderings showing ribbons (magenta) within cone pedicles (gray) from WT and G369i KI mice. ***b,*** 3D renderings show ribbon sites in a WT cone pedicle contacting one horizontal (HC1; yellow) and three bipolar cells (BC1-3; purple). ***b',*** Raw image from *b* shows a single plane example of BC1-2 and HC1 contacting the ribbon site. ***c-d'***, Single plane raw (*c,d*) images and 3D reconstructions (*c',d'*) show ribbon sites within the G369i KI cone pedicle contacting in *c,c'*: horizontal cells (HC1-2) only (upper panels), CBCs (BC1-2) only (lower panels); and in *d,d'*: a glial cell (orange) and an unknown partner. The glial cell completely envelops the pedicle. Inset in *d'* shows glial-contacting ribbon site (arrow). In other panels, arrows indicate points of contact between ribbons and other postsynaptic elements.

Figure 8. Patch clamp recordings of light responses of horizontal cells in WT, G369i KI and Ca_v1.4 KO mice. *a-b*, Representative traces from whole-cell patch clamp recordings of horizontal cells held at -70 mV (*a*) and quantified data (*b*) for currents evoked by 1 s light flashes (λ = 410 nm) plotted against light intensities. In *b*, peak current amplitudes during (ON Response) and after (OFF Response) the light stimuli were plotted against photon flux per μm^2 ($\Phi_q/\mu m^2$). Data represent mean ± SEM. WT, n = 8; G369i KI, n = 13; Ca_v1.4 KO, n = 8. There was a significant difference in responses of WT, G369i KI, and Ca_v1.4 KO horizontal cells. For ON responses, F(16, 216) = 22, p <0.0001 by two-way repeated measures ANOVA, Tukey's

multiple comparisons post-hoc test. For OFF responses, $F(16, 216) = 13.61$, $p < 0.0001$ by two-way repeated measures ANOVA, Tukey's multiple comparisons post-hoc test. ***c-d*,** Representative traces from horizontal cells held at -70 mV (*c*) and quantified data (*d*) for currents evoked by 1-s light flashes (λ = 410 nm, 1.2 x 10^5 $\Phi_q/\mu m^2$) before, during, and after washout of DNQX (20 μM). In *d,* symbols represent responses from individual cells, n = 5 cells for WT and 3 cells for G369i KI, bars represent mean ± SEM. **, $p < 0.01$ by paired t-tests.

Figure 9. Ca^{2+} imaging of cone terminals in WT and G369i KI mice. Depolarization-evoked fluorescence changes (ΔF) were measured by two-photon imaging of Fluo3-filled cone pedicles labeled with PNA-Alexa 568. ***a*,** Representative images at the indicated timepoints (T) before (control), during, and after (wash) bath application of KCl (50 mM) and KCl+ISR (10 μM). For clarity, PNA-Alexa 568 labeling was outlined (magenta, solid circles) and the actual labeling only shown in the initial panel of images. Dashed, yellow circles represent ROIs for analyses. ***b,*** Changes in cone pedicle Fluo3 fluorescence were normalized to the initial fluorescence intensity at time= 0 ($\Delta F/F_0$). Solid lines and shaded areas represent the mean $\pm$ SEM, respectively. WT, n = 11 pedicles; G369i KI, n = 14 pedicles.

Figure 10. Characterization of ERGs and visual behavior in WT, G369i KI, and $Ca_v1.4$ KO mice. ***a***, Representative traces of photopic ERGs recorded in the presence of background green light (20 cd · s/m^2) in WT, G369i KI and $Ca_V1.4$ KO mice. Flash intensities are shown at left. Arrows and arrowheads depict the a- and b-waves, respectively. ***b***, a-wave (left) and b-wave (right) amplitudes are plotted against light intensity. Symbols and bars represent mean ± SEM. WT, n = 7; G369i KI, n = 5; $Ca_V1.4$ KO, n = 6. *, $p < 0.05$; **, $p < 0.01$; ***, $p < 0.001$; ****, $p < 0.0001$; ns, not significant; Two-way ANOVA with Tukey's posthoc multiple comparisons. ***c,d***, Representative traces (*c*) and quantified data (*d*) for 10 Hz flicker responses evoked by

white light flashes of increasing luminance (from -4 to 2 log cd· s/m^2). Arrows in *c* depict inverted waveform responses in G369i KI mice that are absent in $Ca_v1.4$ KO mice. Symbols and bars represent mean ± SEM. WT, n = 7; G369i KI, n = 5; $Ca_V1.4$ KO, n = 6. *, $p < 0.05$; **, $p < 0.01$. Two-way ANOVA with Tukey's posthoc multiple comparisons. ***e*,** Representative swim path traces of WT, G369i KI and $Ca_V1.4$ KO mice from the visible platform swim tests performed in the dark (scotopic, upper panel) and light (photopic, lower panel). ***f*,** Time required to reach the platform (latency to platform) was compared for each mouse strain. Symbols represent the average of the last 3 swim trials for each mouse of each genotype for both dark and light conditions. Dotted lines represent the mean. WT, n = 11; G369i KI, n = 10; $Ca_V1.4$ KO, n = 9. *, $p < 0.05$; ***, $p < 0.001$; ****, $p < 0.0001$; Kruskal-Wallis one-way ANOVA with Dunn's post hoc analysis.

Supplementary Figures

Figure 2- Figure Supplement 1. Voltage ramps do not reveal I_{Ca} in rods of G369i KI mice. ***a,b***, Representative traces of I_{Ca} evoked by voltage ramps at 0.15 mV/ms (left) or 0.5 mV/ms (right) in rods of WT or G369i KI mice. ***c***, Comparison of current amplitudes evoked by the different voltage ramps in rods of WT and G369i KI mice. Bars represent mean ± SEM. Each point represents a different cell. p-values were determined by unpaired t-test (t(12)=7.428 for 0.15 mV/ms, t(10) = 6.028 for 0.5 mV/ms).

Figure 3- Figure Supplement 2. Effect of ML218 on $Ca_v1.4$ and $Ca_v3.2$ in HEK293T cells. Cells were transfected with $Ca_v1.4$, β_{2x13}, and $\alpha_2\delta$−4 (a-d) or $Ca_v3.2$ (e-h). ***a,e,*** Representative

traces and I-V plots for I_{Ca} evoked by 50 ms steps to +10 mV (a) or 200 ms steps to -35 mV (e) from a holding voltage of -90 mV. Currents were recorded in the presence of vehicle (DMSO) or ML 218 (5 μM for $Ca_v1.4$ and 1 μM for $Ca_v3.2$). ***b,f,*** Left, I-V relationships for data obtained as in *a,e* but using steps to various voltages in a single representative cell. *Right*, Boltzmann fit of the responses, normalized to the maximum I_{Ca} amplitude. ***c,d,g,h***, Graphs depicting effect of ML 218 on V_{half} (c,g) and I_{Ca} amplitude (d,h) ** W=-93.00, Z=-3.1366, p=0.0017; *** W=105.0, Z=3.8419, p=0.0001; both by Wilcoxon matched pairs signed rank test. * t(2)=0.582, p=0.0366 by paired t-test.

Figure 2- Figure Supplement 3. Violin plots showing expression levels of transcripts at the single cell level in the retina of WT and G369i KI mice. Each point represents result from a single cell. a, Expression levels of transcripts known to be expressed in cones. Cells were grouped according to their transcriptional profiles using unsupervised clustering. Clusters 8 and 16 were identified as cones based on their high expression of Arr3, Opn1mw, Opn1sw, and Gnat2. b, Expression of transcripts that encode Cav1.4 (Cacna1f) and Cav3 subtypes (Cacna1g, Cacna1h, Cacna1i) in clusters 8 and 16 in retina from WT and G369i KI mice. In cluster 8, there was a small but significant decrease in the level of Cacna1f in the G369i KI vs WT (*, p = 0.01) but not in cluster 16 (p =0.09). There was no significant difference in the level of Cacna1h between genotypes in cluster 8 or 16 (p = 1).

Methods

Table 3. Key resources used in this study

Primary Antibodies				
Antibody Name (clone/designation)	**Working Concentration**	**Source**	**Identifier**	**RRID**
Bassoon (SAP7F407/Ms monoclonal)	2 μg/mL	ThermoFisher Scientific	MA1-20689	AB_2066981
$Ca_V1.4$ (Rb Polyclonal)	5 μg/mL	Amy Lee	Ab167	AB_2650487

Cone Arrestin (Rb Polyclonal)	1 µg/mL	Millipore	AB15282	AB_1163387
Cone Arrestin-CF647 (Rb Polyclonal)	5 µg/mL	Millipore	AB15282	AB_1163387
CtBP2 (Clone 16/Ms Monoclonal)	1 µg/mL	BD Biosciences	612044	AB_399431
GPR179 (mAB 1a/Ms Monoclonal)	2 µg/mL	Millipore	MAB427	AB_2069582
mGluR6 (366/Ms Monoclonal)	1 µg/mL	Dr. Theodore Wensel (Agosto et al., 2014, 2018)	N/A	N/A
TRPM1 (545H5/Ms Monoclonal)	1 µg/mL	Dr. Theodore Wensel (Agosto et al., 2018)	N/A	N/A
Secondary Antibodies				
Antibody Name and Conjugate	**Working Concentration**	**Source**	**Identifier**	**RRID**
Goat Anti-Mouse IgG1 Alexa Fluor 488	4 µg/mL	ThermoFisher	A-21121	AB_2535764
Goat Anti-Mouse IgG2a Alexa Fluor 555	4 µg/mL	ThermoFisher	A-21137	AB_2535776
Goat Anti-Rabbit Alexa Fluor 555	4 µg/mL	ThermoFisher	A-21429	AB_2535850
Goat Anti-Rabbit Alexa Fluor 647	4 µg/mL	ThermoFisher	A-21245	AB_2535813

Chemicals		
Reagent or Resource	**Source**	**Identifier**
Adenosine 5'-triphosphate magnesium salt	SIGMA	A9187
Agarose, low gelling temperature	Sigma-Aldrich	A0701
AMES	Sigma, US Biological	Sigma: A1420; US Biological: A1372
Antisedan	Zoetis US LLC	10000449
1,2-Bis(2-aminophenoxy)ethane-N,N,N′,N′-tetraacetic acid (BAPTA)	Sigma-Aldrich	A4926
Cadmium Chloride	Sigma	202908
Calcium chloride dihydrate	Sigma-Aldrich	223506
Cesium Chloride	Fisher Bioreagents	BP210
Cesium methanesulfonate	Sigma-Aldrich	C1426
Creatine phosphate, dipotassium salt	EMD Millipore	237911
D-Glucose	Fisher	D16
DL-*threo*-β-Benzyloxyaspartic acid (DL-TBOA)	Tocris	1223
6,7-Dinitroquinoxaline-2,3-dione disodium salt (DNQX)	Abcam	ab120169
Dimethyl sulfoxide	SIGMA	D2650
Dulbecco's Modified Eagle Medium, high glucose	Gibco	11965-092
Dulbecco's Phosphate Buffered Saline, no calcium, no magnesium	Gibco	14190-144
Ethylene glycol-bis(2-aminoethylether)-N,N,N',N'-tetraacetic acid (EGTA)	Sigma-Aldrich	03777
Fetal Bovine Serum (FBS)	Gibco	16140-071
FuGENE HD Transfection reagent	Promega	E2311
Guanosine 5'-triphosphate sodium salt hydrate	Sigma-Aldrich	G8877
4-(2-Hydroxyethyl)piperazine-1-ethanesulfonic acid (HEPES)	SIGMA	H3375
Systane Hypromellose lubricant eye gel	Alcone	300650474016

Isradipine	Sigma-Aldrich	I6658
Ketamine Injection C IIIN 100 mg/mL	Dechra Veterinary Products, LLC	17033-100-10
Magnesium Chloride hexahydrate	SIGMA	M2393
Methanesulfonic acid	Sigma-Aldrich	471356
Mix-n-Stain Antibody Labeling Kit	Biotium	92238
ML218 Hydrochloride	Tocris	4507
N-Methyl-D-glucamine (NMDG)	Sigma-Aldrich	66930
Nickel Chloride	Sigma	339350
Optimal Cutting Temperature compound	Sakura	4583
Penicillin-Streptomycin	Sigma-Aldrich	P0781
Picrotoxin	Tocris	1128
Sigmacote	Sigma-Aldrich	SL2-25mL
Sodium Bicarbonate	MACRON	7412-12
Sodium phosphate monobasic anhydrous	Sigma	S3139
Sodium phosphate dibasic anhydrous	Sigma	RDD022
Sodium Chloride, Crystal	MACRON	7581-12
Potassium Chloride	Fisher Chemical	P217
Sodium hydroxide	Fisher chemical	S318
Sodium lactate	Sigma-Aldrich	1614308
Sodium malate	Sigma-Aldrich	1613881
Sodium pyruvate	Sigma-Aldrich	P2256
Sodium succinate	Sigma-Aldrich	S9637
Strychnine HCl	Sigma	S8753
(3*S*)-3-[[3-[[4-(Trifluoromethyl)benzoyl]amino]phenyl]methoxy]-L-aspartic acid (TBF-TBOA)	Tocris	2532
Tetraethylammonium chloride (TEA-Cl)	Sigma-Aldrich	86614
TRIS	VWR	0497
Tropicamide ophthalmic solution 1%	Akorn, Inc.	17478-0102-12
Trypsin-EDTA (0.05%), phenol red	Gibco	25300054
Anased (Xylazine) Injection 100 mg/mL	Pivetal	46066-0750-02
4-Ethylphenylamino-1,2-dimethyl-6-methylaminopyrimidinium chloride (ZD7288)	Tocris	1000

Experimental Models: Organisms/Strains

Reagent or Resource	**Source**	**Identifier**	**RRID**
HEK293T	ATCC	CRL-3216	CVCL_0063
Mouse: C57BL/6J	Jackson Labs	000664	IMSR_JAX:000664
Mouse: G369i KI	A. Lee [17]	N/A	N/A
Mouse: $Ca_V1.4$ KO	Jackson Labs	017761	IMSR_JAX:017761
Ground Squirrel	TLC	--	--

Software and Algorithms

Reagent or Resource	**Source**	**Identifier**
Amira	ThermoFisher Scientific	https://www.thermofisher.com/amira
cellSens	Olympus	https://www.olympus-lifescience.com/en/software/cellsens
Espion software	Diagnosys, Inc.	https://info.diagnosysllc.com/software
FLUOVIEW	Olympus	https://www.olympus-lifescience.com/en/laser-scanning/fv3000
GraphPad Prism	GraphPad	https://www.graphpad.com
IGOR Pro	WaveMetrics	https://www.wavemetrics.com

ImageJ	NIH	https://imagej.nih.gov/ij
pClamp	Molecular Devices	https://www.moleculardevices.com
Patchmaster	Harvard Bioscience, Inc.	https://www.heka.com
ScanImage	MBF Biosciences	https://docs.scanimage.org/index.html

Animals

All mouse and macaque experiments were performed in accordance with guidelines approved by the National Institutes of Health and the Institutional Animal Care and Use Committees at the University of Texas at Austin. All ground squirrel (*Ictidomys tridecemlineatus*) procedures performed at Northwestern University were approved by the Institutional Animal Care and Use Committee. The G369i KI [17] and $Ca_v1.4$ KO mouse strains were bred on the C57BL6/J background strain for at least 10 generations. Adult male and female mice were used (6-12 weeks old), and aged-matched C57BL6/J mice were used as the control (WT) animals.

Immunofluorescence

Mice between 6-8 weeks of age were anesthetized using isoflurane and euthanized by cervical dislocation. Eyes were enucleated and hemisected. The eye cups with retina were fixed on ice in 4% paraformaldehyde in 0.1 M phosphate buffer (PB) for 30 min. Fixed eye cups were then washed three times with 0.1 M PB containing 1% glycine followed by infusion of 30% sucrose at 4°C overnight. The eye cups were orientated along their dorsal-ventral axis and frozen in a 1:1 (wt/vol) mixture of Optimal Cutting Temperature compound and 30% sucrose in a dry ice/isopentane bath. Eye cups were cryosectioned at 20 µm on a Leica CM1850 cryostat (Leica Microsystems), mounted on Superfrost plus Micro Slides (VWR), dried for 5 to 10 min at 42°C, and stored at -20°C until used. Slides with mounted cryosections were warmed to room temperature, washed with 0.1 M PB for 30 min to remove the OCT/sucrose mixture and blocked

with dilution solution (DS, 0.1 M PB/10% goat serum/0.5% Triton-X100) for 15 min or overnight at room temperature. All remaining steps were carried out at room temperature. All primary antibodies and appropriate secondary antibodies were diluted in DS at concentrations specified in the Key Resources Table (Table 3). Sections were incubated with primary antibodies for 1 h or overnight and then washed five times with 0.1 M PB. Sections were then incubated with secondary antibodies for 30 min and then washed five times with 0.1 M PB. Trace 0.1 M PB was removed, and sections were then mounted with #1.5H coverslips (ThorLabs) using ProLong Glass Antifade Mountant with or without NucBlue (Thermo Fisher Scientific).

For double labeling with other rabbit polyclonal antibodies, CAR antibodies were conjugated with the CF647 fluorophore (CAR-647) using the Mix-n-Stain antibody labeling kit according to the manufacturer's protocol (Biotium). Sections were processed first with rabbit polyclonal $Ca_v1.4$ or EAAT2 antibodies and corresponding secondary antibodies as described above. To prevent CAR-647 from binding to any available sites on the anti-rabbit secondary antibodies previously added to the sections, $Ca_V1.4$ or EAAT2 antibodies were readded to the sections and incubated for 30 min. After washing, the sections were incubated with CAR-647 for 1 h, followed by wash steps and cover glass mounting.

Immunofluorescence in labeled retinal sections was visualized using an Olympus FV3000 confocal microscope (Tokyo, Japan) equipped with an UPlanApo 60x oil HR objective (1.5 NA). Images were captured using the Olympus FLUOVIEW software package. Acquisition settings were optimized using a saturation mask to prevent signal saturation prior to collecting 16-bit. All confocal images presented are maximum z-projections. Images (256 x 256 pixels) used in analyses of synaptic proteins were collected using a 30X optical zoom, 0.6 Airy disk aperture, and voxel size of $0.028\,\mu m \times 0.028\,\mu m \times 0.2\,\mu m$ $(X \times Y \times Z)$. Amira segmentation was used for generating 3D binary masks, and Amira 3D label analysis was used for quantification of immunofluorescent and masked images. Non-deconvolved images were used for all analyses. 3D binary masks of individual CAR-labeled pedicles were made by setting the

threshold 1 standard deviation above mean fluorescence intensity of each 3D image. 3D binary masks of presynaptic labels (CtBP2, $Ca_V1.4$, and Bassoon) or postsynaptic labels (GPR179, mGluR6, and TRPM1) within or associated with the pedicle, respectively, were made by setting the threshold 3 standard deviations above the mean fluorescence intensity. To aid in presentation, high-mag images displayed in Figs.1b and 6a were deconvolved using cellSens software (Olympus), and any immunofluorescence corresponding to rod synaptic proteins was subtracted from the image.

Molecular biology and transfection

The cDNAs for $Ca_V1.4$ (GenBank: NM_019582), β_{2X13} (GenBank: KJ789960), and $\alpha_2\delta$-4 (GenBank: NM_172364) were previously cloned into pcDNA3.1 [66]. The cDNA for $Ca_V3.2$ (GenBank: AF051946) was a gift from Dr. Edward Perez-Reyes, University of Virginia. All constructs were verified by DNA sequencing before use. Human embryonic kidney 293T (HEK293T) cells were cultured in Dulbecco's Modified Eagle's Medium with 10% FBS at 37°C in 5% CO_2. At 70–80% confluence, the cells were co-transfected with cDNAs encoding human $Ca_v1.4$ (1.8 μg) β_{2X13} (0.6 μg), $\alpha_2\delta$-4 (0.6 μg), and enhanced GFP in pEGFP-C1 (Clonetech, 0.1 μg) or $Ca_V3.2$ (2 μg) and pEGFP-C1 (0.1 μg) using FuGENE 6 transfection reagent according to the manufacturer's protocol. Cells treated with the transfection mixture were incubated at 37°C for 24 hr, dissociated using Trypsin-EDTA, and replated at a low density to isolate single cells. Replated cells were then incubated at 30°C or 37°C for an additional 24 hr before beginning experiments.

Solutions for patch clamp recordings

HEK293T extracellular recording solution contained the following (in mM): 140 Tris, 20 $CaCl_2$, 1 $MgCl_2$, pH 7.3 with methanesulfonic acid, osmolarity 309 mOsm/kg. HEK293T internal

recording solution contained the following: 140 NMDG, 10 HEPES, 2 $MgCl_2$, 2 Mg-ATP, 5 EGTA, pH 7.3 with methanesulfonic acid, osmolarity 358 mOsm/kg.

For recordings of I_{Ca} in mouse retina, extracellular recording solution contained the following (in mM): 115 NaCl, 2.5 KCl, 22.5 $NaHCO_3$, 1.25 NaH_2PO_4, 2 $CaCl_2$, 1 $MgCl_2$, 5 HEPES, 5 CsCl, 5.5 Glucose, osmolarity 290 mOsm/kg. Mouse cone intracellular solution contained the following (in mM): 105 $CsMeSO_4$, 20 TEA-Cl, 1 $MgCl_2$, 11 HEPES, 10 EGTA, 4 Mg-ATP, 10 phosphocreatine, 0.3 Na-GTP, pH 7.4 with CsOH, osmolarity 300 mOsm/kg.

For recordings of I_{Ca} in ground squirrel retina, extracellular recording solution contained the following (in mM): 10 HEPES, 85 NaCl, 3.1 KCl, 2.48 $MgSO_4$, 6 Glucose, 1 Na-succinate, 1 Na-malate, 1 Na-lactate, 1 Na-pyruvate, 2 $CaCl_2$, 25 $NaHCO_3$, and 20 TEA-Cl, osmolarity 285 ± 5 mOsm/kg. Intracellular solution contained the following (in mM): 80 CsCl, 10 BAPTA, 2 $MgSO_4$, 10 HEPES, 20 TEA-Cl, 5 Mg-ATP, and 0.5 Na-GTP, pH 7.35 with CsOH, osmolarity 285 ± 5 mOsm/kg. For recordings of I_{Aglu}**,** extracellular recording solution contained (in mM): 125 NaCl, 3.0 KCl, 1.25 NaH_2PO_4, 25 $NaHCO_3$, 2 $CaCl_2$, 1 $MgCl_2$, 3 dextrose, 3 sodium pyruvate, 0.1 picrotoxin and 0.02 DNQX, and in indicated experiments 0.0013 TFB-TBOA. Intracellular I_{Aglu} contained (in mM): 125 KSCN, 10 TEA-Cl, 10 HEPES, 1 $CaCl_2$, 2 $MgCl_2$, 0.3 Na-GTP, 4 Mg-ATP, 10 K_2 phosphocreatine, 0.02 ZD7288. Mouse and ground squirrel extracellular slice recording solutions were equilibrated with 5% CO_2 / 95% O_2 to a pH of ~7.5.

For recordings of light responses in horizontal cells of mouse retina, extracellular recording solution consisted of Ames' media supplemented with 100 U/mL penicillin, 0.1 mg/mL streptomycin and 22.6 mM $NaHCO_3$, osmolarity 280 ± 5 mOsm/kg. The intracellular recording solution contained the following (in mM): 135 K-Aspartate, 10 KCl, 10 HEPES, 5 EDTA, 0.5 $CaCl_2$, 1 Mg-ATP, 0.2 Na-GTP, pH 7.35 with KOH, osmolarity 305 ± 5 mOsm/kg.

Table 4. Pharmacological drugs and their concentrations used in electrophysiological recordings of cones.

Compound	Concentration (μM) for mouse recordings	Concentration (μM) for ground squirrel recordings
Cadmium	200	N/A
DL-TBOA	N/A	375
DNQX	20	N/A
Isradipine	1	2
ML218	5	5
Nickel	100	N/A
Picrotoxin	N/A	50
Strychnine	N/A	10
ZD7288	N/A	50
Glutamate	1000	N/A

Patch clamp electrophysiology

Whole-cell voltage clamp recordings of transfected HEK293T cells were performed 48 to 72 hrs after transfection using an EPC-10 amplifier and Patchmaster software (HEKA Elektronik, Lambrecht, Germany). Patch pipette electrodes with a tip resistance between 4 and 6 MΩ were pulled from thin-walled borosilicate glass capillaries (World Precision Instruments, Sarasota, FL) using a P-97 Flaming/Brown Puller (Sutter Instruments, Novato, CA). A reference Ag/AgCl wire was placed into the culture dish mounted on an inverted Olympus IX70 microscope. Recordings were performed at room temperature. A pressurized perfusion pencil multi-barrel manifold controlled with Valve Bank II (AutoMate Scientific, Inc., Berkeley, CA) was used to deliver extracellular solutions. ML218 of different concentrations (0.5, 1, 5, 25 and 100 mM) was added to the extracellular solution the day of experiments. Series resistance was compensated up to 70%, and passive membrane leak subtraction was conducted using a P/−4 protocol. Whole-cell Ca^{2+} currents (I_{Ca}) of transfected HEK293T cells were evoked for 50 ms with incremental +5 mV steps from -80 mV to +65 mV. Current-Voltage (IV) data were fit with a single Boltzmann equation: $I_{Ca} = G_{max}(V_m-V_r)/(1+\exp[-(V_m-V_h))/k])$, where G_{max} is the maximal conductance, V_m is the test voltage, V_r is the Ca^{2+} reversal potential, V_h is the membrane

potential required to activate 50% of G_{max}, and k is the slope factor. Data were sampled at 100 kHz, filtered at 3 kHz, and analyzed using custom programs written in IgroPro (WaveMetrics).

Whole-cell voltage clamp recordings of mouse cones, rods, and horizontal cells and macaque cone terminals were performed using an EPC-10 amplifier and Patchmaster software (HEKA). Patch pipette electrodes with a tip resistance between 10 and 14 MΩ for cones and 6-8 for horizontal cells were pulled from thick-walled borosilicate glass (1.5 mm outer diameter; 0.84 mm inner diameter; World Precision Instruments).

To prepare retinal slices, adult mice (6 – 8 weeks old) were anesthetized using isoflurane and euthanized by cervical dislocation. Eyes were enucleated, placed into cold Ames' media slicing solution, and hemisected. Following removal of the vitreous, the eye cup was separated into dorsal and ventral halves using a scalpel. Ventral retina was isolated, molded into low-melt agarose and mounted in a Leica VT1200s vibratome (Leica Biosystems). Mouse retina slicing solution was continuously bubbled with 100% O_2 and contained the following: Ames' Medium with L-glutamine supplemented with (in mM) 15 NaCl, 10 HEPES, 10 U/mL penicillin, 0.1 mg/mL streptomycin, pH 7.4, osmolarity 300 mOsm/kg. Vertical (~200 µm) or horizontal (~160 µm) retinal slices were anchored in a recording chamber, placed onto a fixed stage, and positioned under an upright Olympus BX51WI microscope equipped with a 60X water-immersion objective (1.0 NA), and superfused with extracellular solution (flow rate of ~1-2 ml/min) at room temperature. Slices were visualized using IR-DIC optics and an IR-2000 (Dage MTI, Michigan City, IN) or SciCam Pro (Scientifica, Uckfield, United Kingdom) CCD camera controlled by the IR-capture software package or µManager, respectively [67, 68]. Drugs used in these experiments were added to the mouse extracellular solution the day of experiments at the concentration described in Table 4. A reference Ag/AgCl pellet electrode was placed directly into the recording chamber solution. Data from whole-cell recordings with a series resistance >20 MΩ were discarded.

Cone and rod somas were identified based on their morphology and location. Cone identity was confirmed by the whole-cell capacitance (~3-4 pF), which is larger than rod whole-cell capacitance (~0.7-1 pF). Unless otherwise indicated, cones and rods were held at -90 mV for 200 ms followed by a ramp of +0.5 mV/ms to +40 mV. To determine voltage activation of I_{Ca}, whole-cell Ca^{2+} currents in cones were evoked for 50 ms with incremental +5 mV steps from -80 mV to +40 mV. The activation voltage of I_{Ca} is reported as G/G_{max}, where G is the conductance at each test voltage and G_{max} is the maximum peak conductance for each cone. Conductance was calculated using the equation $I_{Ca} = G(V_m-V_r)$, where V_r is +60 mV. To determine steady state inactivation of I_{Ca}, currents in cones were evoked for 500 ms with incremental +5 mV steps from -90 mV and -30 mV followed by a final step to -30 mV for 50 ms after each test voltage. The steady state inactivation of I_{Ca} is reported as I/I_{max}, where I is the peak current in the final voltage step to -30 mV and I_{max} is the maximum peak current for each cone. Data were sampled between 20 and 60 kHz and filtered at 3 kHz.

For horizontal cell light responses, horizontal slices were prepared from central mouse retina. The identity of horizontal cells was determined based on their larger soma diameter (~15 µm) compared to bipolar cell somas (~6 µm). During whole cell patch clamp recordings, horizontal cells were held at -70 mV. Light stimuli (1 s) at 410 nm (630 x 830 µm) were presented onto the retina (at a minimum of 5 s intervals) through the microscope's condenser using a Polygon1000 DMD pattern illuminator (Mightex, Pleasanton, CA, USA) and a custom-built light path. Light intensity (in watts) was measured at the point on the microscope stage where the retina is placed using a power meter (Thorlabs, Newton, New Jersey, USA). Photon flux Φ_q (photons/s) within the light stimulus area was calculated using the measured light intensities in the formula:

$$\Phi_q \text{ per } \mu m^2 = \frac{measured\ light\ intensity\ (W)}{\frac{hc}{\lambda}} / light\ stimulus\ area\ (\mu m^2)$$

where *h* is Planck's constant (J*s), *c* is the speed of light (m/s), and λ is the wavelength (m). Light stimulus intensity was increased in Log2 steps from 4.9×10^2 to 2.1×10^5 $\Phi_q/\mu m^2$. For each light intensity step, both ON and OFF current amplitudes were measured from baseline (averaged 5 ms of current prior to light onset) to the maximum positive (after light onset) or maximum negative (after light offset) current, respectively. To confirm the identity of these horizontal cell light responses as AMPA-mediated currents, 1 s light stimuli (410 nm, 1.2×10^5 $\Phi_q/\mu m^2$) were continuously delivered every 10 s before, during and after bath application of 20 μM DNQX.

For voltage clamp recordings of 13-lined ground squirrel cones, retinal slices were prepared as previously described [69]. The eyecup was divided along the dorsal to ventral axis into superior, middle, and inferior parts. The dorsal area above the line of the optic nerve head was defined as superior, the central region with a width of about 5 mm just ventral to the optic nerve head was middle, and the remaining ventral area was inferior. Isradipine and ML218, alone or in combination, were applied from separate puffer pipettes whose orifices were aimed at the cone synaptic region. Recordings were made with an Axopatch 200B amplifier (Molecular Devices). Signals were electronically filtered at 5 kHz and digitized at a rate of 10 kHz. Additional Gaussian filtering was added (cutoff frequency of 500 Hz). Tissue was viewed through a 63x water immersion objective on a Zeiss Axioskop FS2 microscope and superfused with extracellular solution at room temperature. Drugs and their concentrations used during these experiments are described in Table 4. Membrane potential was continuously maintained at -85 mV. During ramp stimulation, the membrane potential was depolarized to -85 to +35 mV at a rate of 1 mV/ms.

For rhesus macaque cone terminal recordings, a 12-year-old male was sedated with ketamine (5 mg/kg I.M.) and dexmedetomidine (0.015 mg/kg I.M.). Post-sedation, the animal received buprenorphine (0.02 mg/kg I.M.), atropine (0.02 mg/kg I.M.), and maropitant citrate (1 mg/kg S.Q.). The animal was intubated and maintained with inhaled isoflurane (0.75-2.0%) and propofol (7-8 mg/kg/hr I.V.). Crystalloid fluids (5 mL/kg/hr) were administered I.V., and phenylephrine (5-10 mcg/kg/hr I.V.) was used for blood pressure support. The animal was under anesthesia for approximately 3 hours prior to perfusion. Transcardial perfusion was approached through a midline thoracotomy. Immediately prior to perfusion, 5 mL of Euthasol® (sodium pentobarbital 390 mg/mL/phenytoin sodium 50 mg/mL) was administered I.V. The descending thoracic aorta was clamped, the pericardium was opened, and the right atrium was cut. The apex of the left ventricle was sharply incised, and a large bore cannula (Yankauer suction handle, 5 mm internal diameter) was inserted through the left ventricle until it could be palpated in the ascending aorta. The cannula was clamped in place at the apex of the left ventricle. The animal was perfused with 4 L of cold phosphate-buffered saline at ~500 mL/min. Eyes were removed approximately 1 hour following perfusion. Eyes were dissected, and eye cups were allowed to dark adapt for ~30 min and stored in bicarbonate buffered Ames' media at 32°C equilibrated with 95% O_2/5% CO_2 prior to slice preparations. Vertical sections of central retina were prepared from 5 mm retina punches as described for mice.

Single cell RNA sequencing

Retinas from 2 WT and 2 G369i KI mice (2-3 month old, all males) were dissected in ice-cold Dulbecco's Phosphate Buffered Saline (D-PBS) and dissociated into single cells using the Papain Dissociation System (Worthington Biochemical). Two retinas were incubated in a 2.5 ml of dissociation solution (40 U/ml papain, 2 mM L-cysteine, 200 U/ml DNAse in Earle's Balanced Salt Solution, EBSS) for 8 min at 37 °C. Following aspiration, 2 ml of inactivation solution

(ovomucoid protease inhibitor and bovine serum albumin (BSA), 10 mg/ml each in EBSS) was added prior to trituration with a series of fire-polished, siliconized glass Pasteur pipettes. The solution was passed through a 40 μm mesh (pluriStrainer, Cat# 43-50040-51, pluriSelect) prior to centrifugation (200 x *g* for 5 min, 4 °C). Following aspiration of the supernatant, the cell pellet was resuspended in 0.5 ml D-PBS+0.5% BSA. Cell suspensions (10,000 cells per sample) were loaded on the Chromium Controller (10X Genomics) and processed for cDNA library generation following the manufacturer's instructions for the Chromium NextGEM Single Cell 3' Reagent Kit v3.1 (10X Genomics). The resulting libraries were examined for size and quality using the Bioanalyzer High Sensitivity DNA Kit (Agilent) and their concentrations were measured using the KAPA SYBR Fast qPCR kit (Roche). Samples were sequenced on the NovaSeq 6000 instrument (paired end, read 1: 28 cycles, read 2: 90 cycles) with a targeted depth of 9K reads/cell.

scRNA-seq Fastq files were processed with CellRanger (v7.1.0) using the reference genome mm10–2020-A with introns included. CellRanger outputs were imported to Seurat (v5.0.1), gene by feature count matrix was constructed, log normalization was performed, and the log normalized values were used for downstream analysis. Unsupervised clustering was performed in Seurat using resolution=0.5. DEsingle method (v1.6.0, [70]) was used for differential expression analysis comparing G369i KI to WT in each cluster.

Serial block-face scanning electron microscopy and 3D reconstructions

Eye cups were prepared from P42 WT and G369i KI littermates and fixed using 4% glutaraldehyde in 0.1M cacodylate buffer, pH 7.4, for 4 hours at room temperature followed by additional fixation overnight at 4°C. Glutaraldehyde-fixed eye cups were then washed 3 times in 0.1M cacodylate buffer. Retinas were thereafter isolated and embedded in Durcupan resin after staining, dehydration, and embedding as described previously (Della Santina et al., 2016). A

Thermo Scientific VolumeScope serial block face scanning electron micrscope was used to image embedded retinas. Retinal regions comprising a 2x2 montage of 40.96 μm tiles were imaged at a resolution of 5nm/pixel and section thickness of 50 nm. Image stacks were aligned, and cone photoreceptor terminals reconstructed using TrakEM2 (NIH). Postsynaptic partners at cone ribbons were followed to the inner nuclear layer to determine their identity. Amira software was used for 3D visualization of reconstructed profiles.

Electroretinography

Retinal function was assessed using the Celeris system (Diagnosys, Inc.) paired with the Espion software (Diagnosys, Inc.). Mice were anaesthetized under red light (660 nm) via intraperitoneal (I.P.) injection with ketamine/xylazine mixture (100 mg/kg ketamine, 10 mg/kg xylazine). Tropicamide ophthalmic solution (1 %) and hypromellose lubricant eye gel (0.3 %) were administered topically to both eyes before the mouse was secured to a heated (37 °C) platform to maintain body temperature. Ag/AgCl corneal stimulators were placed on each eye. After collecting data from individual mice, atipamezole (Antisedan, 1-2 mg/kg) was I.P. injection administered to reverse the effects of the ketamine and xylazine. For photopic ERGs, eyes were light adapted using a background green light at 20 cd·s/m^2 for 10 min. Following light adaptation, eight different light intensity pulses (-0.5, 0, 0.5, 1, 1.5, 2, 2.3 and 2.6 log cd·s/m^2) were delivered on top of the background green light. ERG a-waves were measured from baseline to the peak of the negative potential. ERG b-waves were measured without filtering the oscillatory potentials from the peak of the a-wave to the peak of the positive potential within 60-70 ms (WT) and 80- 100 ms (G369i KI and $Ca_V1.4$ KO) of the light stimuli. For flickering ERGs, mice were dark adapted (>12 h). White light pulses from -4 to 2.5 log cd·s/m^2 were delivered in 0.5 log unit steps at 10 Hz. Response amplitudes were measured from the trough to the peak of each response at all light intensities. Each intensity stimulus was delivered 10 times, with a 3 s

interval between each stimulus, and averaged. The mean response amplitudes recorded in the right and left eye of each mouse are reported for all quantified ERG data.

Visible platform swim test

The visible platform swim test was performed as has been previously described [29]. WT, G369i KI, and $Ca_v1.4$ KO male and female mice (6- 9 weeks old) were dark-adapted overnight and allowed to adapt to the procedure room for at least 1 h prior to beginning the experiments. A water-filled, 4-foot diameter galvanized steel tank and a visible white platform with a diameter of 10 cm was used for the swim test. Mice were subjected to 6 swim trials per day. Assays conducted under photopic (55 lux) and scotopic conditions (0 lux) were performed on days 1 and 2, respectively. Light intensity for photopic and scotopic conditions was measured at the platform using an Extech HD450 light meter (FLIR Systems, Nashua, New Hampshire). Mice were given 90 s to find the platform before being removed. After one trial was performed on all mice, the platform was moved to one of three different locations, top left, top center, and top right in relation to the initial site of mouse placement in tank. Each trial was recorded using an infrared camera (Basler AG, Ahrensburg, Germany) and EthoVision XT16 software (Noldus Information Technology). Locating the platform was considered successful when mice contacted the platform with a head-on approach, even if mice failed to escape onto the platform. Mice were allowed to rest on the platform for 15 s at the end of each trial before being returned to a pre-warmed cage. Latency to find the platform was manually recorded and confirmed using recorded videos. Male and female mice were tested separately, and no sex differences in performance were identified post-hoc using two-way RM-ANOVA (Supplementary Table 1). Male and female data were combined into a single group for each genotype. Latency to platform was calculated by averaging the final 3 trials under scotopic and photopic conditions for each mouse and compared using Kruskal-Wallis one-way ANOVA with Dunn's posthoc multiple comparison test.

Ca^{2+} Imaging of Cone Terminals

Retinas were dissected and stored in oxygenated mouse retina slicing solution. The loading of the cell-permeant Ca^{2+} dye Fluo-3, AM was modified from on a previous publication[71]. To label the base of cone terminals, retinas were incubated in retina slicing solution containing PNA Lectin conjugated with CF568 (100 μg/mL) for 15 min at room temperature. Then the retinas were incubated with retina slicing solution containing 1mM Fluo-3, AM and 0.025% pluronic acid (Biotium) for 45 min at room temperature followed by 3 rinses with retina slicing solution. The retinas were then incubated in retina slicing solution for 15 min at 35ºC to increase esterase activity. Vertical retina slices were prepared as described above. Slices were mounted on a Hyperscope multiphoton system (Scientifica, Uckfield, United Kingdom) equipped with a resonant scanner and a Mai Tai HP DeepSee laser (Spectra-Physics, Milpitas, CA, USA) tuned to 800 nm at 5% power. Slices were perfused with normal extracellular solution containing (in mM) 112 NaCl, 3 KCl, 1 $MgCl_2$, 3 $CaCl_2$, 1.25 NaH_2PO_4, 10 Na Pyruvate, 22.5 $NaHCO_3$, 5 HEPES, 10 Glucose, osmolarity 300 $\pm$ 5 mOsm/kg. High-K+ extracellular solution contained (in mM) 65 NaCl, 50 KCl, 1 $MgCl_2$, 3 $CaCl_2$, 1.25 NaH_2PO_4, 10 Na Pyruvate, 22.5 $NaHCO_3$, 5 HEPES, 10 Glucose, osmolarity 300 $\pm$ 5 mOsm/kg. Extracellular solutions were supplemented with 20 μM CNQX, 25 μM L-APV, and 100 μM picrotoxin. Isradipine (10 μM) was added to High-K+ extracellular solution. Images (512x512) were collected as 15-frame averages at 0.93 Hz using ScanImage (MBF Bioscience, Williston, VT, USA). Changes of Fluo-3 fluorescence in cone terminals were measured in ROIs drawn juxtaposed to PNA-CF568 labeling using Fiji[72].

Data analysis

Electrophysiological data were analyzed by custom routines written in IgorPro software (Wavemetrics) and statistical analysis was performed using Prism software (GraphPad). Data

were analyzed for normality by Shapiro Wilk test followed by parametric (t-test or ANOVA) or non-parametric methods (Kruskal Wallis, Mann-Whitney, Wilcoxon).

References

1. Haverkamp, S., Grunert, U. & Wassle, H. The cone pedicle, a complex synapse in the retina. *Neuron* **27**, 85-95 (2000).

2. Mercer, A.J. & Thoreson, W.B. The dynamic architecture of photoreceptor ribbon synapses: cytoskeletal, extracellular matrix, and intramembrane proteins. *Vis Neurosci* **28**, 453-471 (2011).

3. Frederick, C.E. & Zenisek, D. Ribbon Synapses and Retinal Disease: Review. *Int J Mol Sci* **24** (2023).

4. Mansergh, F.*, et al.* Mutation of the calcium channel gene Cacna1f disrupts calcium signaling, synaptic transmission and cellular organization in mouse retina. *Hum Mol Genet* **14**, 3035-3046 (2005).

5. Liu, X.*, et al.* Dysregulation of $Ca_v1.4$ channels disrupts the maturation of photoreceptor synaptic ribbons in congenital stationary night blindness type 2. *Channels* **7**, 514-523 (2013).

6. Chang, B.*, et al.* The nob2 mouse, a null mutation in Cacna1f: anatomical and functional abnormalities in the outer retina and their consequences on ganglion cell visual responses. *Vis Neurosci* **23**, 11-24 (2006).

7. Singh, A., *et al.* C-terminal modulator controls Ca^{2+}-dependent gating of $Ca_v1.4$ L-type Ca^{2+} channels. *Nat Neurosci* **9**, 1108-1116 (2006).

8. Wahl-Schott, C., *et al.* Switching off calcium-dependent inactivation in L-type calcium channels by an autoinhibitory domain. *Proc. Natl. Acad. Sci. U. S. A.* **103**, 15657-15662 (2006).

9. Bech-Hansen, N.T., *et al.* Loss-of-function mutations in a calcium-channel a_1-subunit gene in Xp11.23 cause incomplete X-linked congenital stationary night blindness. *Nature Genet.* **19**, 264-267 (1998).

10. Strom, T.M., *et al.* An L-type calcium-channel gene mutated in incomplete X-linked congenital stationary night blindness. *Nature Genet.* **19**, 260-263 (1998).

11. Waldner, D.M., Bech-Hansen, N.T. & Stell, W.K. Channeling Vision: CaV1.4-A Critical Link in Retinal Signal Transmission. *Biomed Res Int* **2018**, 7272630 (2018).

12. Boycott, K.M., Pearce, W.G. & Bech-Hansen, N.T. Clinical variability among patients with incomplete X-linked congenital stationary night blindness and a founder mutation in CACNA1F. *Can J Ophthalmol* **35**, 204-213 (2000).

13. Zeitz, C., Robson, A.G. & Audo, I. Congenital stationary night blindness: an analysis and update of genotype-phenotype correlations and pathogenic mechanisms. *Progress in retinal and eye research* **45**, 58-110 (2015).

14. Regus-Leidig, H., *et al.* Photoreceptor degeneration in two mouse models for congenital stationary night blindness type 2. *PLoS One* **9**, e86769 (2014).

15. Zabouri, N. & Haverkamp, S. Calcium channel-dependent molecular maturation of photoreceptor synapses. *PLoS One* **8**, e63853 (2013).

16. Raven, M.A.*, et al.* Early afferent signaling in the outer plexiform layer regulates development of horizontal cell morphology. *J Comp Neurol* **506**, 745-758 (2008).

17. Maddox, J.W.*, et al.* A dual role for Cav1.4 Ca(2+) channels in the molecular and structural organization of the rod photoreceptor synapse. *Elife* **9**, e62184 (2020).

18. Perez-Reyes, E. Molecular physiology of low-voltage-activated t-type calcium channels. *Physiol Rev* **83**, 117-161 (2003).

19. Davison, A., Lux, U.T., Brandstatter, J.H. & Babai, N. T-Type Ca(2+) Channels Boost Neurotransmission in Mammalian Cone Photoreceptors. *J. Neurosci.* **42**, 6325-6343 (2022).

20. Koschak, A.*, et al.* Cav1.4alpha1 subunits can form slowly inactivating dihydropyridine-sensitive L-type Ca2+ channels lacking Ca2+-dependent inactivation. *J. Neurosci.* **23**, 6041-6049 (2003).

21. Williams, B., Maddox, J.W. & Lee, A. Calcium Channels in Retinal Function and Disease. *Annu Rev Vis Sci* (2022).

22. Martemyanov, K.A. & Sampath, A.P. The Transduction Cascade in Retinal ON-Bipolar Cells: Signal Processing and Disease. *Annu Rev Vis Sci* **3**, 25-51 (2017).

23. Hack, I., Frech, M., Dick, O., Peichl, L. & Brandstatter, J.H. Heterogeneous distribution of AMPA glutamate receptor subunits at the photoreceptor synapses of rodent retina. *Eur J Neurosci* **13**, 15-24 (2001).

24. Brandstatter, J.H., Koulen, P. & Wassle, H. Selective synaptic distribution of kainate receptor subunits in the two plexiform layers of the rat retina. *J. Neurosci.* **17**, 9298-9307 (1997).

25. Feigenspan, A. & Babai, N. Functional properties of spontaneous excitatory currents and encoding of light/dark transitions in horizontal cells of the mouse retina. *Eur J Neurosci* **42**, 2615-2632 (2015).

26. Krizaj, D. Calcium stores in vertebrate photoreceptors. *Adv Exp Med Biol* **740**, 873-889 (2012).

27. Nusinowitz, S., Ridder, W.H., 3rd & Ramirez, J. Temporal response properties of the primary and secondary rod-signaling pathways in normal and Gnat2 mutant mice. *Exp Eye Res* **84**, 1104-1114 (2007).

28. Vinberg, F., Wang, T., Molday, R.S., Chen, J. & Kefalov, V.J. A new mouse model for stationary night blindness with mutant Slc24a1 explains the pathophysiology of the associated human disease. *Hum Mol Genet* **24**, 5915-5929 (2015).

29. Bimonte-Nelson, H., Daniel, J. & Koebele, S. *The maze book: theories, practice, and protocols for testing rodent cognition* (Springer, 2015).

30. Beier, C., *et al.* Deafferented Adult Rod Bipolar Cells Create New Synapses with Photoreceptors to Restore Vision. *J. Neurosci.* **37**, 4635-4644 (2017).

31. Shen, N., Wang, B., Soto, F. & Kerschensteiner, D. Homeostatic Plasticity Shapes the Retinal Response to Photoreceptor Degeneration. *Curr Biol* **30**, 1916-1926 e1913 (2020).

32. Leinonen, H., *et al.* Homeostatic plasticity in the retina is associated with maintenance of night vision during retinal degenerative disease. *Elife* **9** (2020).

33. Care, R.A., *et al.* Mature Retina Compensates Functionally for Partial Loss of Rod Photoreceptors. *Cell rep* **31**, 107730 (2020).

34. Kiyonaka, S., *et al.* RIM1 confers sustained activity and neurotransmitter vesicle anchoring to presynaptic Ca2+ channels. *Nat Neurosci* **10**, 691-701 (2007).

35. Kiyonaka, S., *et al.* Physical and functional interaction of the active zone protein CAST/ERC2 and the beta-subunit of the voltage-dependent Ca(2+) channel. *Journal of biochemistry* **152**, 149-159 (2012).

36. tom Dieck, S., *et al.* Molecular dissection of the photoreceptor ribbon synapse: physical interaction of Bassoon and RIBEYE is essential for the assembly of the ribbon complex. *J Cell Biol* **168**, 825-836 (2005).

37. Alpadi, K., *et al.* RIBEYE recruits Munc119, a mammalian ortholog of the Caenorhabditis elegans protein unc119, to synaptic ribbons of photoreceptor synapses. *J. Biol. Chem.* **283**, 26461-26467 (2008).

38. Haeseleer, F. Interaction and colocalization of CaBP4 and Unc119 (MRG4) in photoreceptors. *Invest Ophthalmol Vis Sci* **49**, 2366-2375 (2008).

39. Haeseleer, F.*, et al.* Essential role of Ca^{2+}-binding protein 4, a $Ca_v1.4$ channel regulator, in photoreceptor synaptic function. *Nat Neurosci* **7**, 1079-1087 (2004).

40. Schmitz, F., Konigstorfer, A. & Sudhof, T.C. RIBEYE, a component of synaptic ribbons: a protein's journey through evolution provides insight into synaptic ribbon function. *Neuron* **28**, 857-872 (2000).

41. tom Dieck, S.*, et al.* Deletion of the presynaptic scaffold CAST reduces active zone size in rod photoreceptors and impairs visual processing. *J. Neurosci.* **32**, 12192-12203 (2012).

42. Macosko, E.Z.*, et al.* Highly Parallel Genome-wide Expression Profiling of Individual Cells Using Nanoliter Droplets. *Cell* **161**, 1202-1214 (2015).

43. Koschak, A.*, et al.* a_{1D} ($Ca_v1.3$) subunits can form L-type Ca^{2+} channels activating at negative voltages. *J. Biol. Chem.* **276**, 22100-22106 (2001).

44. Tringham, E.*, et al.* T-type calcium channel blockers that attenuate thalamic burst firing and suppress absence seizures. *Sci Transl Med* **4**, 121ra119 (2012).

45. Cai, S., Gomez, K., Moutal, A. & Khanna, R. Targeting T-type/CaV3.2 channels for chronic pain. *Transl Res* **234**, 20-30 (2021).

46. Garcia-Caballero, A.*, et al.* The deubiquitinating enzyme USP5 modulates neuropathic and inflammatory pain by enhancing Cav3.2 channel activity. *Neuron* **83**, 1144-1158 (2014).

47. Welsby, P.J.*, et al.* A mechanism for the direct regulation of T-type calcium channels by Ca2+/calmodulin-dependent kinase II. *J. Neurosci.* **23**, 10116-10121 (2003).

48. Gomez, K.*, et al.* Cdk5-Dependent Phosphorylation of Ca(V)3.2 T-Type Channels: Possible Role in Nerve Ligation-Induced Neuropathic Allodynia and the Compound Action Potential in Primary Afferent C Fibers. *J. Neurosci.* **40**, 283-296 (2020).

49. Ingram, N.T., Sampath, A.P. & Fain, G.L. Voltage-clamp recordings of light responses from wild-type and mutant mouse cone photoreceptors. *J. Gen. Physiol.* **151**, 1287-1299 (2019).

50. Dembla, E., Dembla, M., Maxeiner, S. & Schmitz, F. Synaptic ribbons foster active zone stability and illumination-dependent active zone enrichment of RIM2 and Cav1.4 in photoreceptor synapses. *Sci Rep* **10**, 5957 (2020).

51. Spiwoks-Becker, I., Glas, M., Lasarzik, I. & Vollrath, L. Mouse photoreceptor synaptic ribbons lose and regain material in response to illumination changes. *Eur J Neurosci* **19**, 1559-1571 (2004).

52. Regus-Leidig, H., Specht, D., Tom Dieck, S. & Brandstatter, J.H. Stability of active zone components at the photoreceptor ribbon complex. *Mol Vis* **16**, 2690-2700 (2010).

53. Sheets, L., Kindt, K.S. & Nicolson, T. Presynaptic CaV1.3 channels regulate synaptic ribbon size and are required for synaptic maintenance in sensory hair cells. *J. Neurosci.* **32**, 17273-17286 (2012).

54. Wong, H.C.*, et al.* Synaptic mitochondria regulate hair-cell synapse size and function. *Elife* **8** (2019).

55. Goel, P.*, et al.* Homeostatic scaling of active zone scaffolds maintains global synaptic strength. *J Cell Biol* **218**, 1706-1724 (2019).

56. Hong, H.*, et al.* Structural Remodeling of Active Zones Is Associated with Synaptic Homeostasis. *J. Neurosci.* **40**, 2817-2827 (2020).

57. Kerov, V.*, et al.* alpha2delta-4 Is Required for the Molecular and Structural Organization of Rod and Cone Photoreceptor Synapses. *J. Neurosci.* **38**, 6145-6160 (2018).

58. Zanetti, L.*, et al.* Function of cone and cone-related pathways in CaV1.4 IT mice. *Sci Rep* **11**, 2732 (2021).

59. Knoflach, D.*, et al.* Ca_v1.4 IT mouse as model for vision impairment in human congenital stationary night blindness type 2. *Channels* **7**, 503-513 (2013).

60. Perez-Reyes, E., Van Deusen, A.L. & Vitko, I. Molecular pharmacology of human Cav3.2 T-type Ca2+ channels: block by antihypertensives, antiarrhythmics, and their analogs. *The Journal of pharmacology and experimental therapeutics* **328**, 621-627 (2009).

61. Snellman, J.*, et al.* Acute destruction of the synaptic ribbon reveals a role for the ribbon in vesicle priming. *Nat Neurosci* **14**, 1135-1141 (2011).

62. Choi, S.Y., Jackman, S., Thoreson, W.B. & Kramer, R.H. Light regulation of Ca2+ in the cone photoreceptor synaptic terminal. *Vis Neurosci* **25**, 693-700 (2008).

63. Bijveld, M.M.*, et al.* Assessment of night vision problems in patients with congenital stationary night blindness. *PLoS One* **8**, e62927 (2013).

64. Peloquin, J.B., Rehak, R., Doering, C.J. & McRory, J.E. Functional analysis of congenital stationary night blindness type-2 CACNA1F mutations F742C, G1007R, and R1049W. *Neuroscience* **150**, 335-345 (2007).

65. Hoda, J.C., Zaghetto, F., Koschak, A. & Striessnig, J. Congenital stationary night blindness type 2 mutations S229P, G369D, L1068P, and W1440X alter channel gating or functional expression of Cav1.4 L-type Ca2+ channels. *J. Neurosci.* **25**, 252-259 (2005).

66. Lee, A.*, et al.* Characterization of Cav1.4 complexes ($\alpha_1$1.4, β_2, and $\alpha_2\delta$−4) in HEK293T cells and in the retina. *J. Biol. Chem.* **290**, 1505-1521 (2015).

67. Edelstein, A., Amodaj, N., Hoover, K., Vale, R. & Stuurman, N. Computer control of microscopes using microManager. *Curr Protoc Mol Biol* **Chapter 14**, Unit14 20 (2010).

68. Edelstein, A.D.*, et al.* Advanced methods of microscope control using muManager software. *J Biol Methods* **1** (2014).

69. DeVries, S.H. & Schwartz, E.A. Kainate receptors mediate synaptic transmission between cones and 'Off' bipolar cells in a mammalian retina. *Nature* **397**, 157-160 (1999).

70. Miao, Z., Deng, K., Wang, X. & Zhang, X. DEsingle for detecting three types of differential expression in single-cell RNA-seq data. *Bioinformatics* **34**, 3223-3224 (2018).

71. Johnson, J.E., Jr.*, et al.* Spatiotemporal regulation of ATP and Ca2+ dynamics in vertebrate rod and cone ribbon synapses. *Mol Vis* **13**, 887-919 (2007).

72. Schindelin, J.*, et al.* Fiji: an open-source platform for biological-image analysis. *Nature methods* **9**, 676-682 (2012).

Figure 1

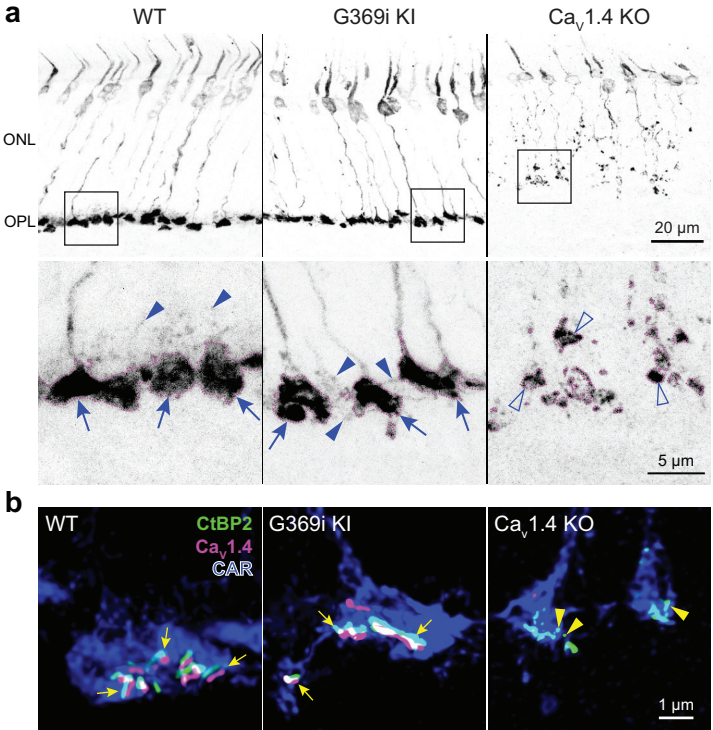
a
WT
G369i KI
Cav1.4 KO
ONL
OPL
20 µm
5 µm
b
WT
CtBP2
Cav1.4
CAR
G369i KI
Cav1.4 KO
1 µm

Figure 2

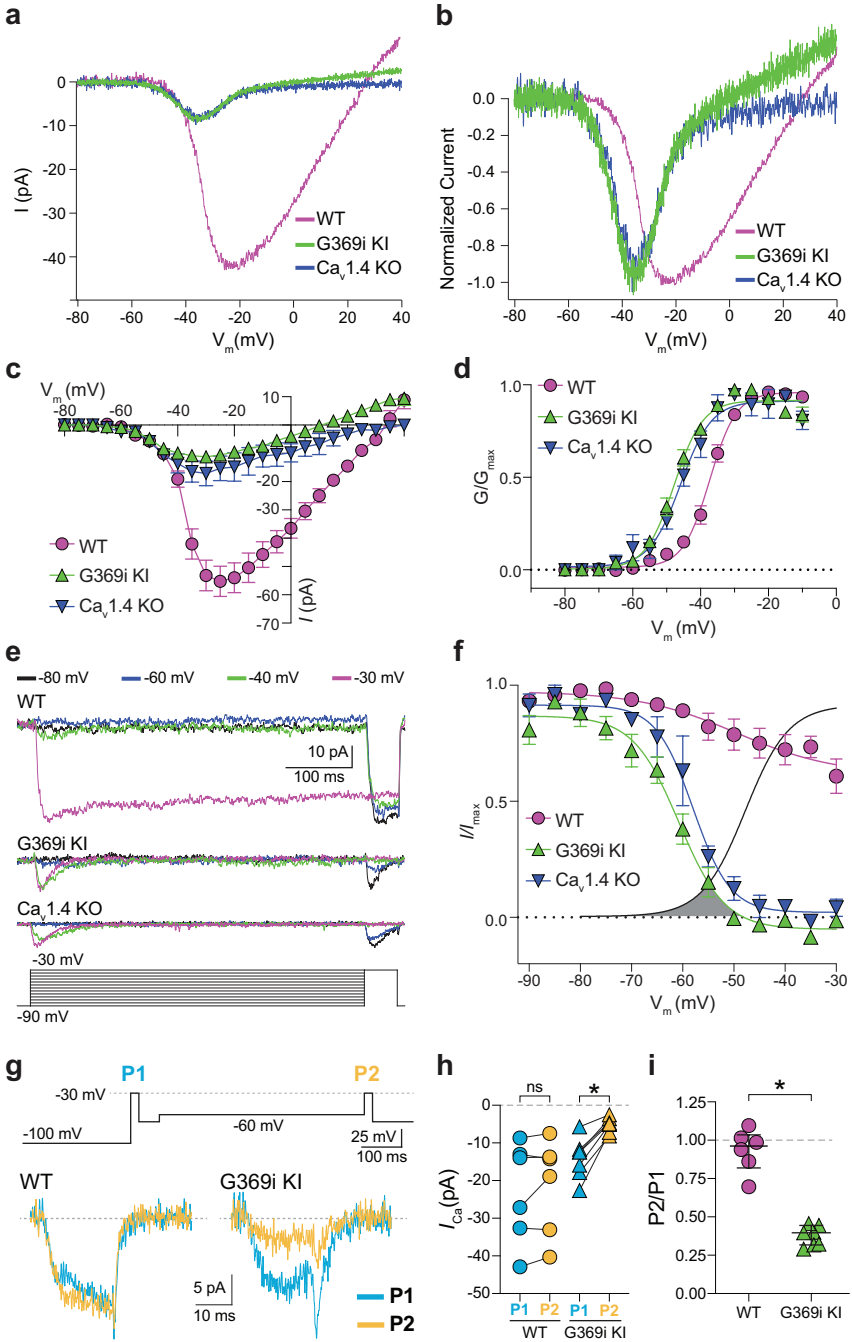
a
I (pA)
WT
G369i KI
Cav1.4 KO
Vm(mV)
b
Normalized Current
WT
G369i KI
Cav1.4 KO
Vm(mV)
c
Vm(mV)
WT
G369i KI
Cav1.4 KO
I (pA)
d
G/Gmax
WT
G369i KI
Cav1.4 KO
Vm (mV)
e
-80 mV
-60 mV
-40 mV
-30 mV
WT
10 pA
100 ms
G369i KI
Cav1.4 KO
-30 mV
-90 mV
f
I/Imax
WT
G369i KI
Cav1.4 KO
Vm (mV)
g
P1
P2
-30 mV
-100 mV
-60 mV
25 mV
100 ms
WT
G369i KI
5 pA
10 ms
P1
P2
h
ns
*
ICa(pA)
P1
P2
P1
P2
WT
G369i KI
i
*
P2/P1
WT
G369i KI

Figure 3

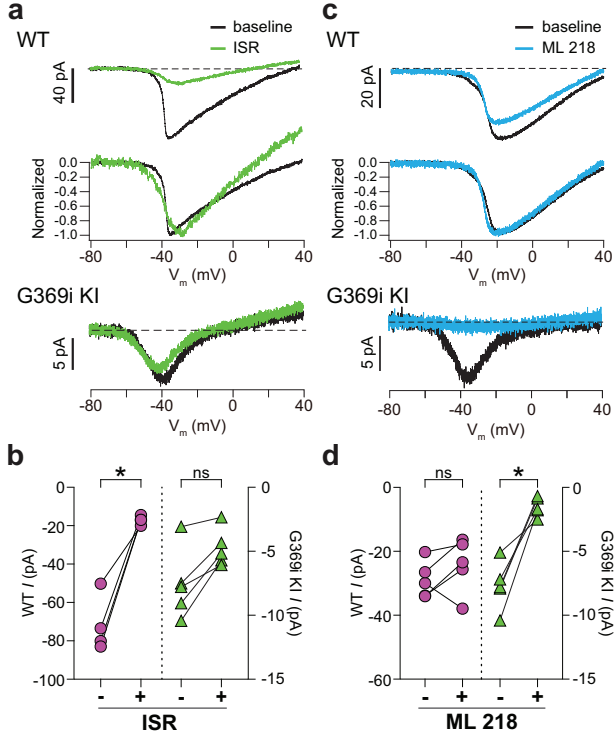
a
WT
baseline
ISR
40 pA
Normalized
0.0
-0.2
-0.4
-0.6
-0.8
-1.0
-80
-40
0
40
V_m (mV)
G369i KI
5 pA
c
WT
baseline
ML 218
20 pA
G369i KI
5 pA
b
*
ns
WT I (pA)
G369i KI I (pA)
ISR
d
ML 218

Figure 4

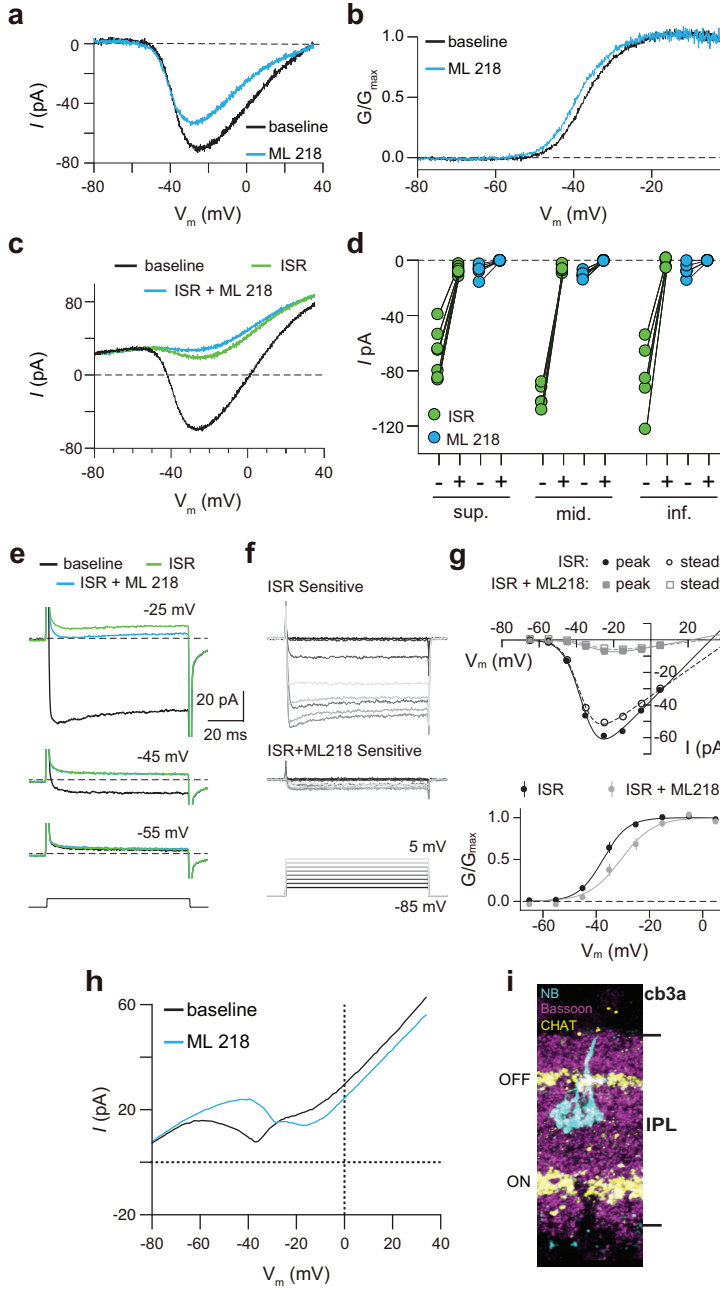
a
I (pA)
baseline
ML 218
V_m (mV)
b
G/G_max
baseline
ML 218
V_m (mV)
c
baseline
ISR
ISR + ML 218
I (pA)
V_m (mV)
d
I pA
ISR
ML 218
sup.
mid.
inf.
e
baseline
ISR
ISR + ML 218
-25 mV
20 pA
20 ms
-45 mV
-55 mV
f
ISR Sensitive
ISR+ML218 Sensitive
5 mV
-85 mV
g
ISR: peak steady
ISR + ML218: peak steady
V_m (mV)
I (pA)
ISR
ISR + ML218
G/G_max
V_m (mV)
h
baseline
ML 218
I (pA)
V_m (mV)
i
NB
Bassoon
CHAT
cb3a
OFF
IPL
ON

Figure 5

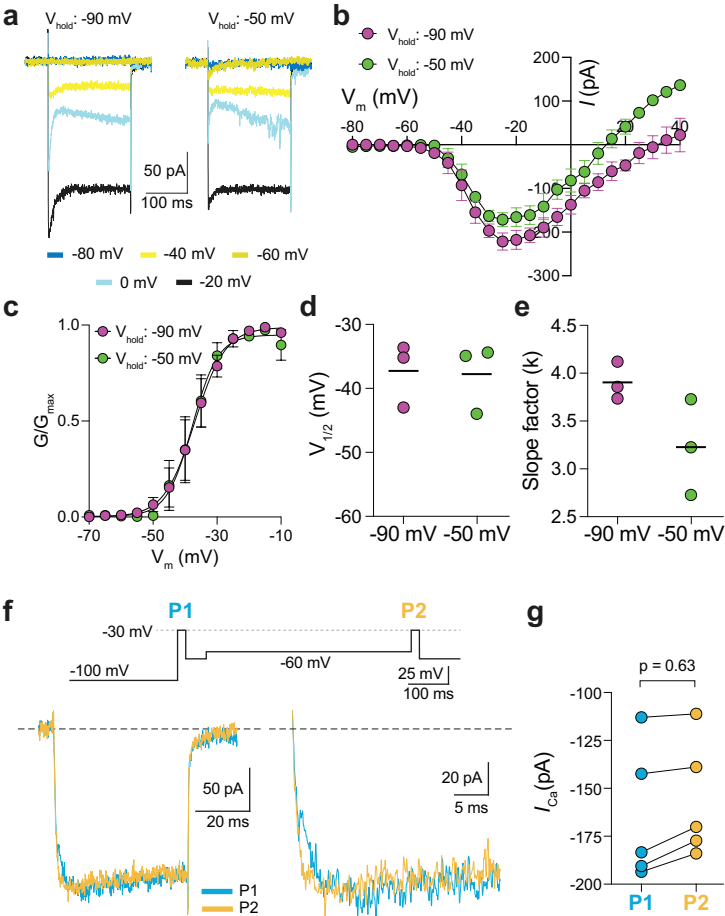
a
V hold: -90 mV
V hold: -50 mV
50 pA
100 ms
-80 mV
-40 mV
-60 mV
0 mV
-20 mV
b
V hold: -90 mV
V hold: -50 mV
V m (mV)
I (pA)
c
G/G max
V m (mV)
d
V 1/2 (mV)
-90 mV
-50 mV
e
Slope factor (k)
-90 mV
-50 mV
f
P1
P2
-30 mV
-100 mV
-60 mV
25 mV
100 ms
50 pA
20 ms
20 pA
5 ms
P1
P2
g
p = 0.63
I Ca (pA)
P1
P2

Figure 6

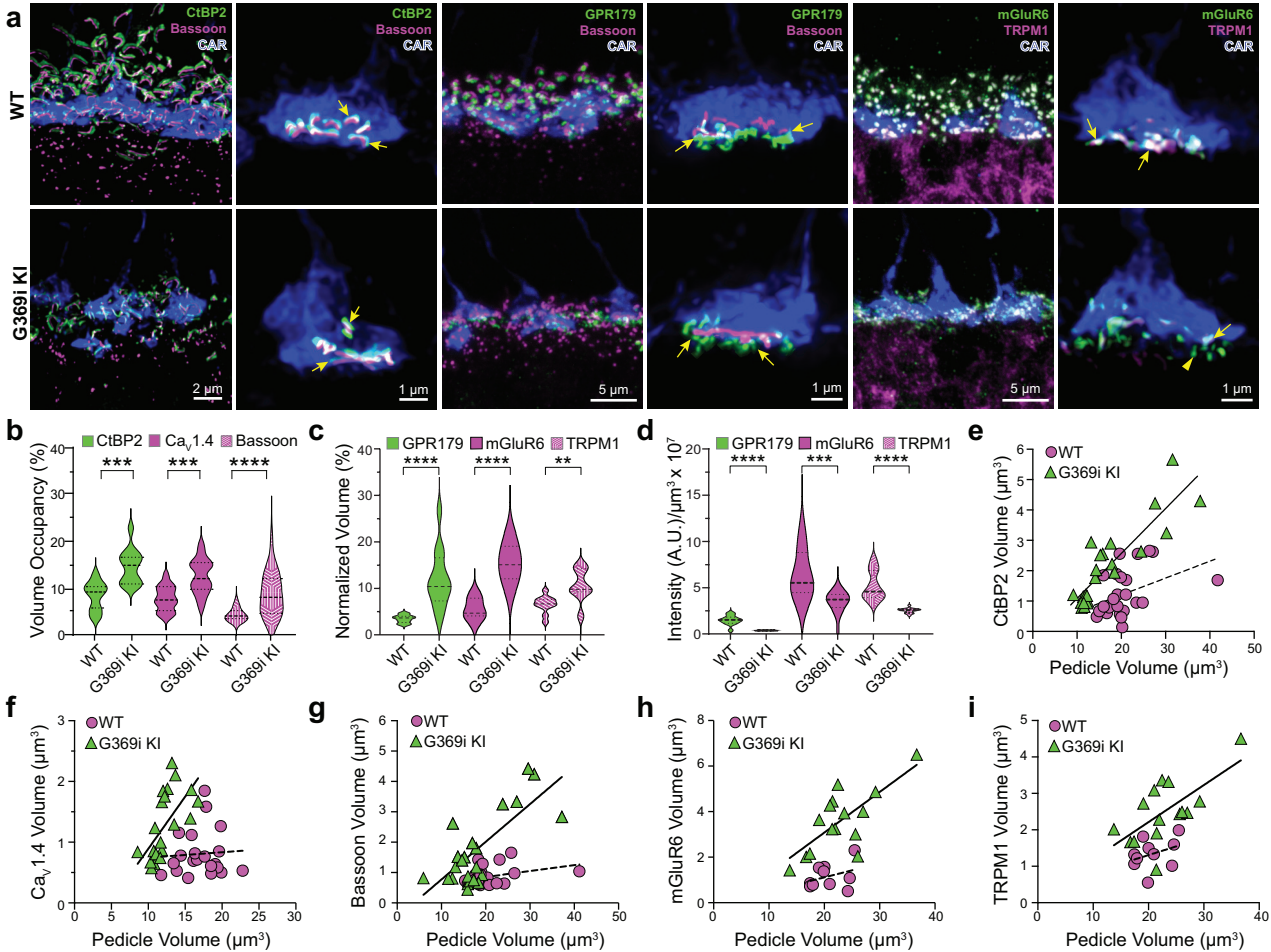
a
WT
G369i KI
CtBP2
Bassoon
CAR
GPR179
mGluR6
TRPM1
2 µm
1 µm
5 µm
b
Volume Occupancy (%)
CtBP2
Cav1.4
Bassoon
c
Normalized Volume (%)
GPR179
mGluR6
TRPM1
d
Intensity (A.U.)/µm³ x 10⁷
e
CtBP2 Volume (µm³)
Pedicle Volume (µm³)
f
Cav1.4 Volume (µm³)
g
Bassoon Volume (µm³)
h
mGluR6 Volume (µm³)
i
TRPM1 Volume (µm³)
WT
G369i KI

Figure 7

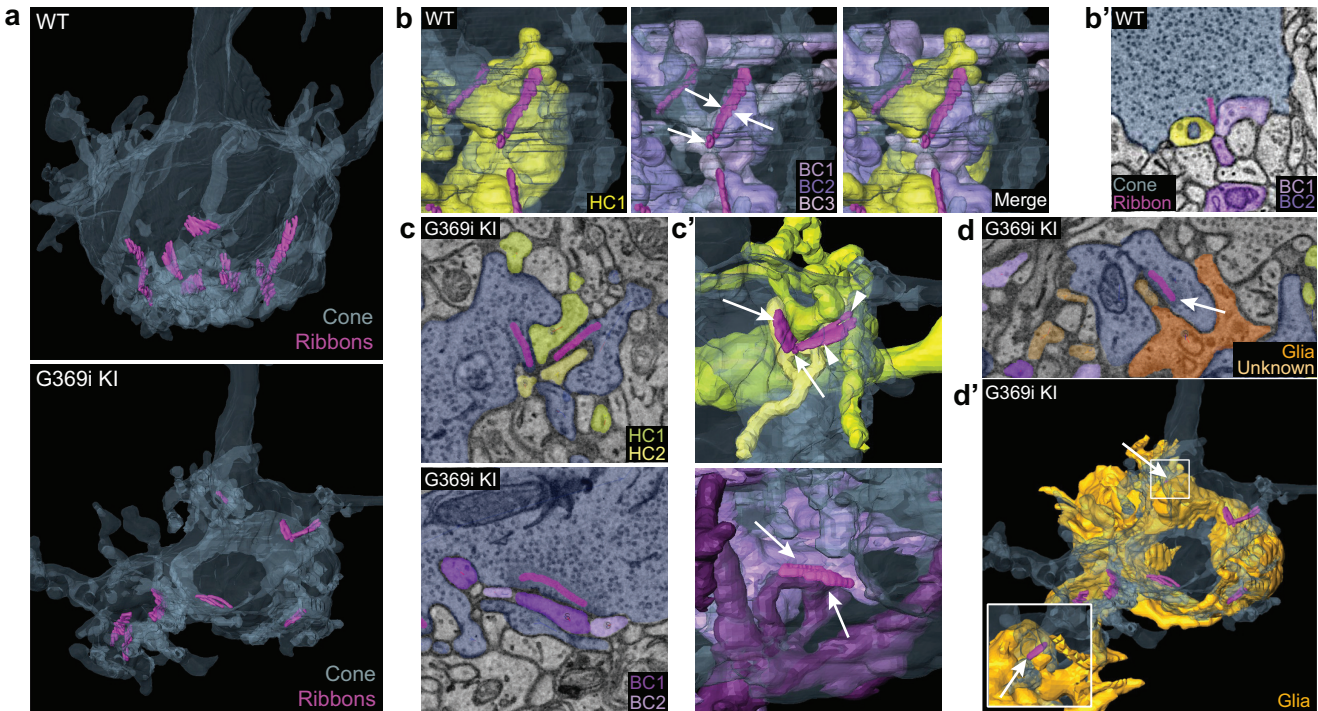
a
WT
Cone
Ribbons
G369i KI
Cone
Ribbons
b
WT
HC1
BC1
BC2
BC3
Merge
b'
WT
Cone
Ribbon
BC1
BC2
c
G369i KI
HC1
HC2
G369i KI
BC1
BC2
c'
d
G369i KI
Glia
Unknown
d'
G369i KI
Glia

Figure 8

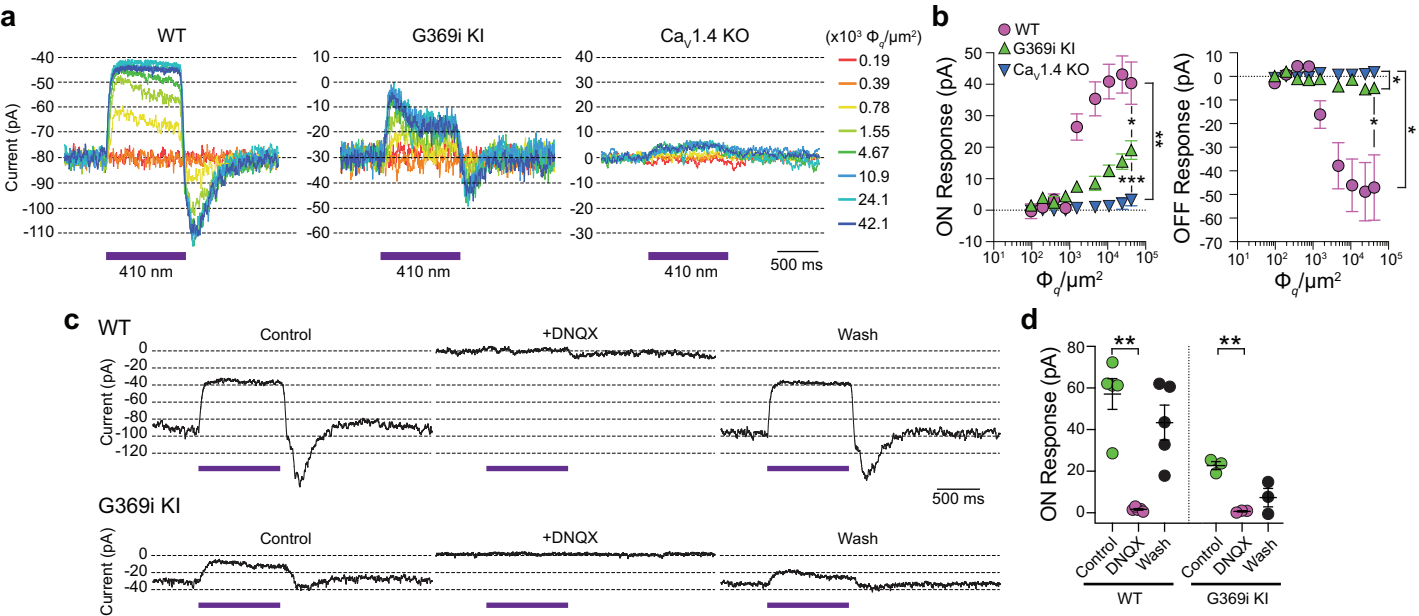
a
WT
G369i KI
Ca$_V$1.4 KO
(x10^3 Φ$_q$/μm^2)
0.19
0.39
0.78
1.55
4.67
10.9
24.1
42.1
Current (pA)
410 nm
500 ms
b
WT
G369i KI
Ca$_V$1.4 KO
ON Response (pA)
OFF Response (pA)
Φ$_q$/μm^2
c
WT
Control
+DNQX
Wash
Current (pA)
500 ms
G369i KI
d
ON Response (pA)
Control
DNQX
Wash
WT
G369i KI

Figure 9

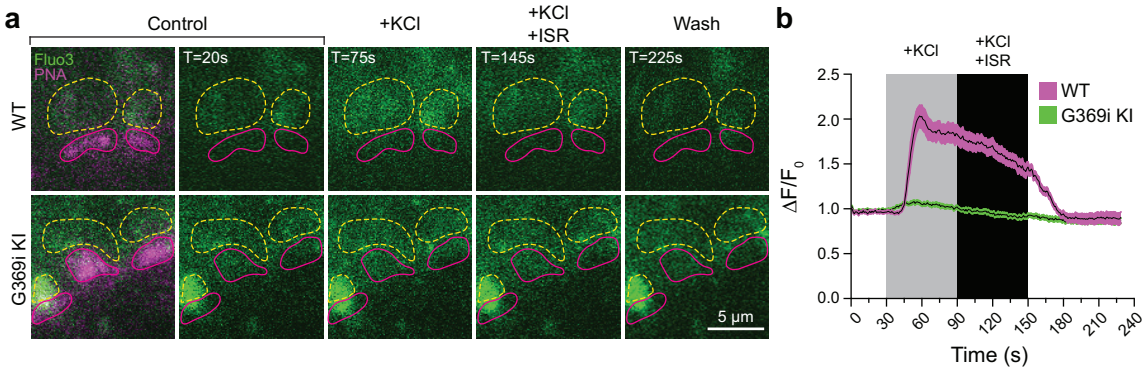
a
Control
+KCl
+KCl
+ISR
Wash
Fluo3
PNA
T=20s
T=75s
T=145s
T=225s
WT
G369i KI
5 µm
b
+KCl
+KCl
+ISR
WT
G369i KI
ΔF/F0
2.5
2.0
1.5
1.0
0.5
0.0
0
30
60
90
120
150
180
210
240
Time (s)

Figure 10

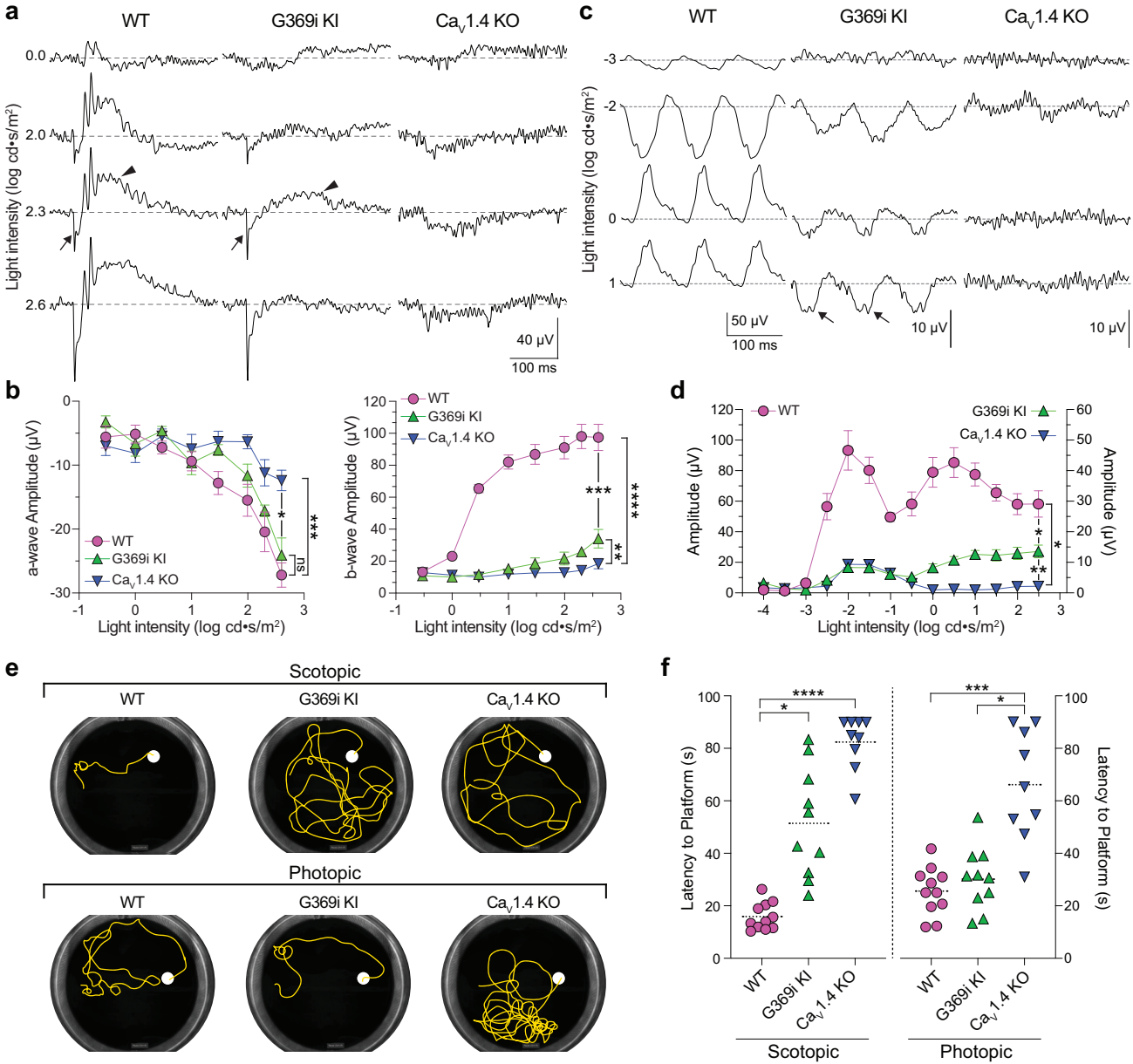
a
WT
G369i KI
Ca$_V$1.4 KO
Light intensity (log cd•s/m²)
0.0
2.0
2.3
2.6
40 µV
100 ms
c
WT
G369i KI
Ca$_V$1.4 KO
Light intensity (log cd•s/m²)
-3
-2
0
1
50 µV
100 ms
10 µV
10 µV
b
a-wave Amplitude (µV)
WT
G369i KI
Ca$_V$1.4 KO
Light intensity (log cd•s/m²)
b-wave Amplitude (µV)
d
Amplitude (µV)
Light intensity (log cd•s/m²)
e
Scotopic
WT
G369i KI
Ca$_V$1.4 KO
Photopic
f
Latency to Platform (s)
WT
G369i KI
Ca$_V$1.4 KO
Scotopic
Photopic